SEA-BED RESPONSE TO NON-BREAKING WAVES

A Thesis

Presented in Partial Fulfillment of the Requirements for

the Degree Bachelor of Science with Distinction in the

College of Engineering of The Ohio State University

By

Jennifer A. Brown

* * * * *

The Ohio State University

2006

Honors Examination Committee:

Diane Foster, Adviser

Thomas C. Lippmann

Keith W. Bedford

Approved by

_____

Adviser

Department of Civil and
Environmental Engineering
and Geodetic Science

ABSTRACT

Despite decades of oceanographic research, there exists a considerable uncertainty in our ability to predict sediment transport and sea-bed geometry in response to free-surface gravity waves. The goal of the multi-institutional collaborative CROss Shore Sediment Transport Experiment (CROSSTEX) was to examine the transport of sediment onshore and offshore in the nearshore region. Observations for this research were obtained in the large scale wave flume at the O.H. Hinsdale Wave Research Laboratory located at Oregon State University in the summer of 2005. The focus of this investigation is on the bed state characteristics (ripple wavelength and height) in response to non-breaking waves. The research method consisted of measuring observations of bedform geometry with a submerged laser-video Particle Image Velocimetry (PIV) system at two water depths offshore of the wave breaking region. Ripple geometry was measured with the strong light reflection from the laser present at the bed captured by the video system. Measurements of ripple wavelength and height were obtained from the PIV images after the sea-bed had responded to the wave climates. The free stream velocity was measured with an Acoustic Doppler Velocimeter (ADV) current meter approximately 30 cm above the bed.

Bed states and ripple types were classified for a range of random wave conditions, with significant wave heights ranging from 30 to 60 cm and wave periods ranging from 4 to 8 sec. Resulting geometries ranged from flat to rippled beds. Two types of ripples were considered: suborbital, defined as having ripple spacing dependent on both wave orbital diameter and sediment grain size, and anorbital, defined as having ripple wavelengths independent of wave orbital diameter. For the range of wave orbital semi-excursion amplitudes and ripple wavelengths observed, *Clifton and Dingler* [1984] would classify the ripple geometries as both suborbital and anorbital at both water depths. However, our results suggest the ripple geometries are purely anorbital at both water depths, and that the anorbital ripple class extends into a smaller range of wave orbital diameters than indicated, consistent with the recent findings of *Crawford and Hay* [2001].

Additional findings include decreasing ripple heights with increasing root-mean-square wave orbital velocity, u_{rms}. In general, no correlations were seen between the ripple geometries and wave periods. Comparisons of ripple geometry to root-mean-square wave orbital velocity, u_{rms}, and significant wave orbital semi-excursion, A, suggest that u_{rms} is a better indicator of when a flat bed will occur. These findings can be used to improve our knowledge of coastal sediment transport and sedimentary structures in the nearshore region.

This is dedicated to my family and friends.

ACKNOWLEDGEMENTS

I wish to thank my adviser, Diane Foster, for introducing me to the world of coastal engineering and giving me the wonderful opportunity to conduct research. Her support and guidance made this thesis possible and has launched my education in a direction I never would have dreamed of exploring.

I thank Claire Nichols for her PIV contributions and for her generous support and Kim Hatton for being a wonderful mentor to me over the years. I would also like to thank the other members of the Ohio State group for providing me with their knowledge over the past year.

I thank Jason Magalen of Oregon State University for his guidance during the experiment and for the help with the sediment analysis. I would also like to thank the staff at the O.H. Hinsdale Wave Research Laboratory at Oregon State University and the other researchers involved in CROSSTEX for providing me with their expertise and assistance.

This research was supported by the Research Experience for Undergraduates program of the National Science Foundation.

TABLE OF CONTENTS

Appendices:

NOTATION

A	significant wave orbital semi-excursion (=d_o/2)
d_o	wave orbital diameter (=2A)
D	median grain diameter
h	water depth
H_{mo}	offshore wave height
L	wave wavelength
T	wave period
u	horizontal fluid velocity
u_{rms}	root-mean-square wave orbital velocity
u_o	significant wave orbital velocity (=2u_{rms})
λ	ripple wavelength
η	ripple height

LIST OF TABLES

LIST OF FIGURES

CHAPTER 1

INTRODUCTION

1.1 Motivation

A more in-depth understanding of coastal processes is required today as a result of the escalating stress being applied to shorelines by the population. The physical role of the beach is to absorb energy from the ocean and act as a buffer between approaching waves and the structures and developments built along the coast. In order to predict larger-scale sediment transport in the nearshore region, knowledge of small-scale sediment processes is needed. An understanding of small-scale sediment developments also provides insight into how ripple formations dissipate wave energy as waves propagate across the continental shelf. This in turn tells us how beaches dissipate the ocean's energy, protecting coastal communities and structures. This research is also valuable to the Navy for interpreting acoustical backscatter when conducting ocean bottom surveys.

Currently, the formation of sedimentary structures in the nearshore is not fully understood. These developments encompass a wide range of morphologic length scales, including small-scale processes occurring in the bottom-boundary-layer, intermediate

scale processes involving sandbar migrations, and large-scale processes of bathymetry evolution. Small-scale processes include both small-scale bedforms that can evolve under large waves at time periods shorter than one wave period, and large-scale bedforms such as lunate megaripples, which are bottom roughness features characterized by deep troughs. Large-scale processes comprise bathymetry changes such as beach erosion and accretion. These morphologic evolutions in the nearshore in turn affect the wave characteristics that determine the small-scale bedform responses. This demonstrates how an understanding of the small-scale sedimentary processes is essential in order to predict large-scale morphologic changes.

At the present time, there exists a considerable uncertainty in our ability to predict the transport of coastal sediments and evolution of sea-bed geometry (or bottom roughness) in response to free surface gravity waves. This is in part due to the complexity of random wave forcing that occurs on natural beaches. Studies conducted in both controlled environments and the field are necessary to obtain observations that can be compared with and used in developing numerical models.

The goal of the experiment conducted was to examine the transport of sediment onshore and offshore in the nearshore region. The focus of this specific investigation is on the bed state characteristics (ripple wavelength and height) in response to non-breaking waves in an intermediate water depth, just seaward of the break point. Observations were obtained during a full scale laboratory study, with alongshore variability limited by the width of the flume. Results from this investigation will be used

to evaluate ripple geometry prediction models that can subsequently be extended to predict morphological evolution in the nearshore.

1.2 Literature Review

These investigations are primarily focused on observations of sedimentary features induced by waves. The observations have been obtained in both the laboratory and the field. The variables in the following discussion have been changed from the original publications to be consistent with the terms used in this paper.

Clifton [1976] proposed a conceptual model of bedform development produced by shoaling waves in nearshore environments. The empirical model was based on a range of field observations from several diverse coastal environments including the swell-swept southern coast of Oregon, the relatively calm southeastern coast of Spain, and the protected sandy shores of Willapa Bay, Washington. By taking fluid density and kinematic viscosity to be constant, and assuming no unidirectional currents and waves of uniform height and period propagating normal to a straight shoreline, the model was reduced to four parameters: maximum wave orbital velocity, u_m, velocity asymmetry, Δu_m, median sediment grain diameter, D, and wave period, T. *Clifton's* [1976] model comprises four main regimes including no sediment movement, symmetric bedforms, asymmetric bedforms, and flat bed. In this model asymmetric bedforms can be described only in qualitative terms due to the uncertainty in applying wave theory to conditions of asymmetric oscillatory currents; therefore asymmetric bedforms will not be considered in this investigation.

According to *Clifton* [1976], the symmetric bedform regime consists of three types of ripples defined by the relations of ripple wavelength to grain size, D, and maximum wave orbital velocity, u_m, at a given wave period, where u_m is related to the diameter of the orbital motion of the wave, d_o, by

$$u_m = \frac{\pi d_o}{T} \tag{1}$$

By creating a plot of the ratio of d_o to D versus the ratio of the ripple wavelength, λ, to the square root of D, the three types of symmetric ripples can be identified, shown in Figure 1.1. *Clifton* [1976] found that at d_o/D values less than about 2000, ripple spacing was independent of grain size and was directly related to the length of the wave orbital diameter; these ripples were termed "orbital" ripples. At d_o/D values greater than 5000, *Clifton* [1976] found that the ripple spacing was largely independent of the wave orbital diameter and was solely dependent on the grain size; these ripples were termed "anorbital" ripples. For d_o/D values between 2000 and 5000, the ripple wavelength may be inversely related to wave orbital diameter but also depends on the grain size; these ripples were termed "suborbital" ripples. The combination of parameters in *Clifton's* [1976] model appears to provide a basis for interpreting wave-formed sedimentary structures; however the model is merely conceptual and still requires further study to be verified.

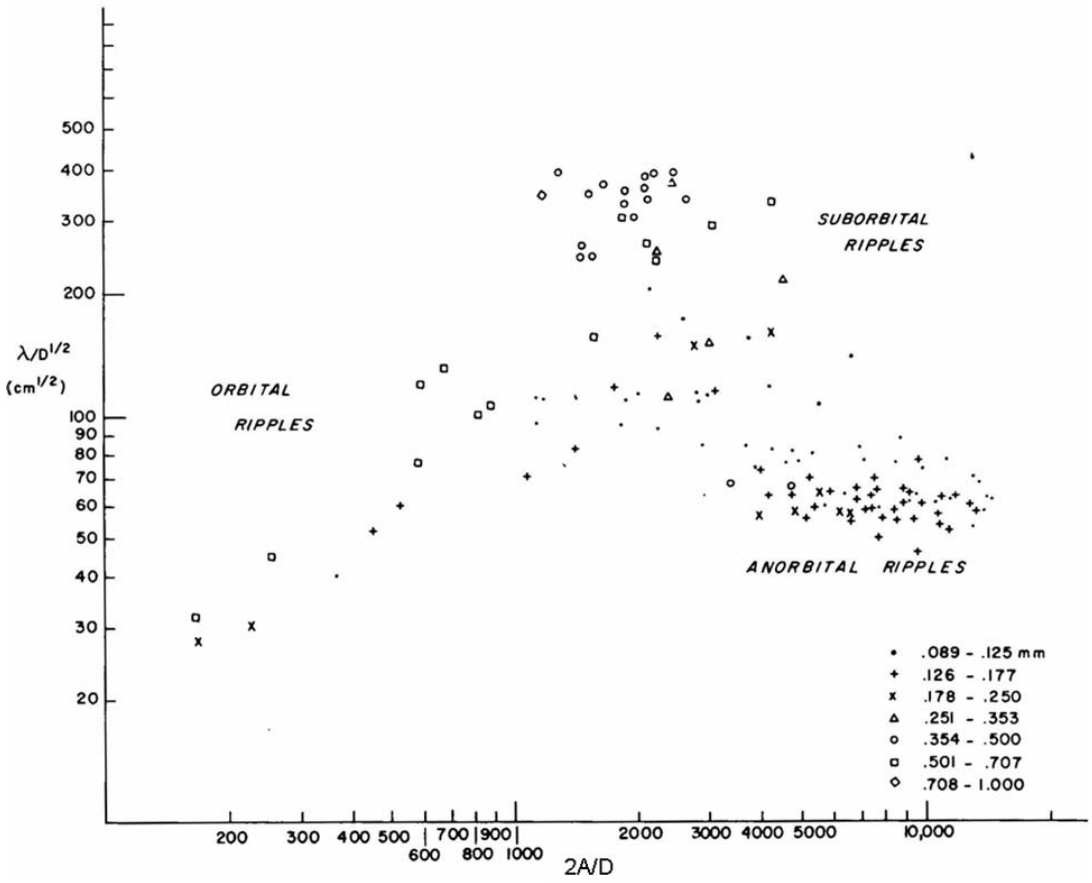

Figure 1.1. Relationship between the normalized wave orbital diameter and ripple wavelength for symmetric ripples. Figure adapted from *Clifton* [1976].

Interpretive models such as *Clifton's* [1976], as well as previously conducted field and laboratory experiments were investigated and summarized by *Clifton and Dingler* [1984]; they used the previously published research to develop a procedure for examining wave-formed sedimentary structures.

In a plot similar to that of *Clifton's* [1976], *Clifton and Dingler* [1984] created a dimensionless plot of d_o/D versus λ/D for a number of field and laboratory studies, seen

in Figure 1.2. Using the larger data set, *Clifton and Dingler* [1984] found similar results as *Clifton* [1976], in that the symmetric ripples can be subdivided into three distinct types, based on the relationship between ripple spacing and wave orbital diameter and grain size.

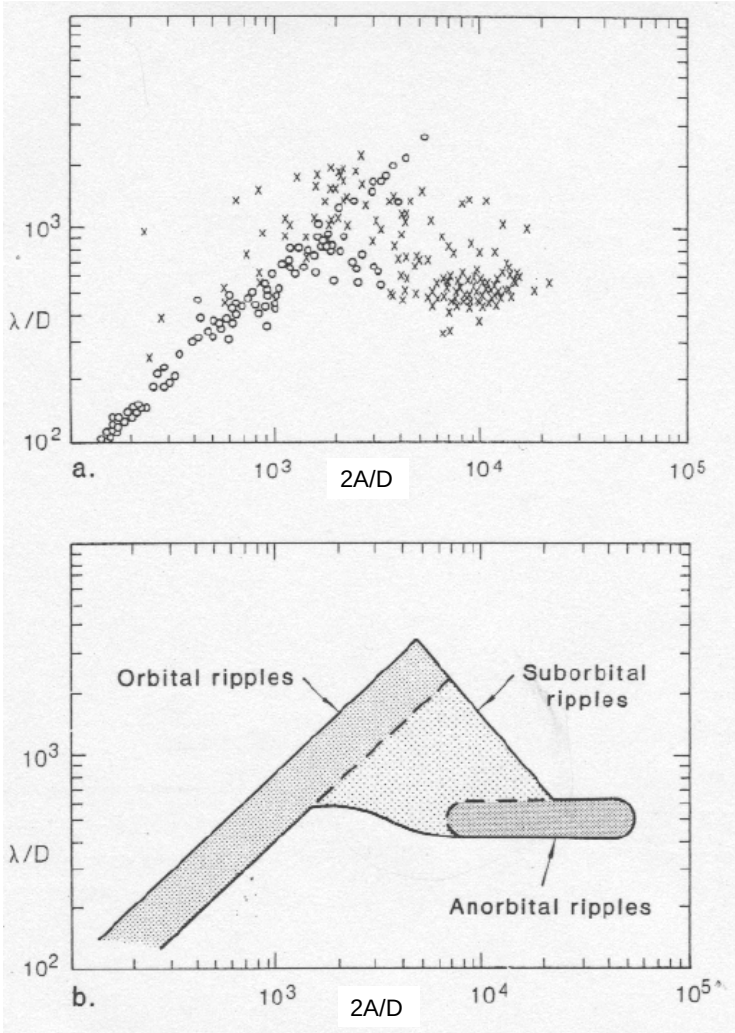

Figure 1.2. Comparisons of the normalized wave orbital diameter to the normalized ripple wavelength. The top panel (a) shows field (crosses) and laboratory (circles) data. The bottom panel (b) shows the proposed ripple classification regimes. Figure adapted from *Clifton and Dingler* [1984].

Clifton and Dingler [1984] concluded that orbital ripples had ripple spacing proportional to the wave orbital diameter in the approximate relationship (*Miller and Komar*, 1980a)

$$\lambda = 0.65 d_o \tag{2}$$

Orbital ripples form under conditions where the d_o/D ratio lies in the range of 100 to 3000 or more, and their λ/D ratio ranges from less than 100 to more than 2000. When the d_o/D ratio is in the range of 1000 to 3000, the ripple spacing decreases as the wave orbital diameter increases; these ripples are of the suborbital type and their ripple spacing depend both on wave orbital diameter and grain size. At d_o/D values greater than 5000, anorbital ripples exist, where the ripple spacing stabilizes at a value independent of wave orbital diameter. Typically, for these ripples, the λ/D ratio is in the range of 400 to 600. These results of *Clifton and Dingler* [1984] typically agree with previous findings and are referenced as a basis for the analysis conducted in this investigation.

Ripple geometry in wave-dominated environments was further investigated by *Wiberg and Harris* [1994], with the focus being on symmetric ripples. The properties of ripples formed under oscillatory flows in both field and flume studies were re-examined in order to construct a method of predicting ripple geometries. The relationship between ripple wavelength and height to wave orbital diameter was examined and is shown in Figure 1.3; the three ripples types discussed earlier are also identified.

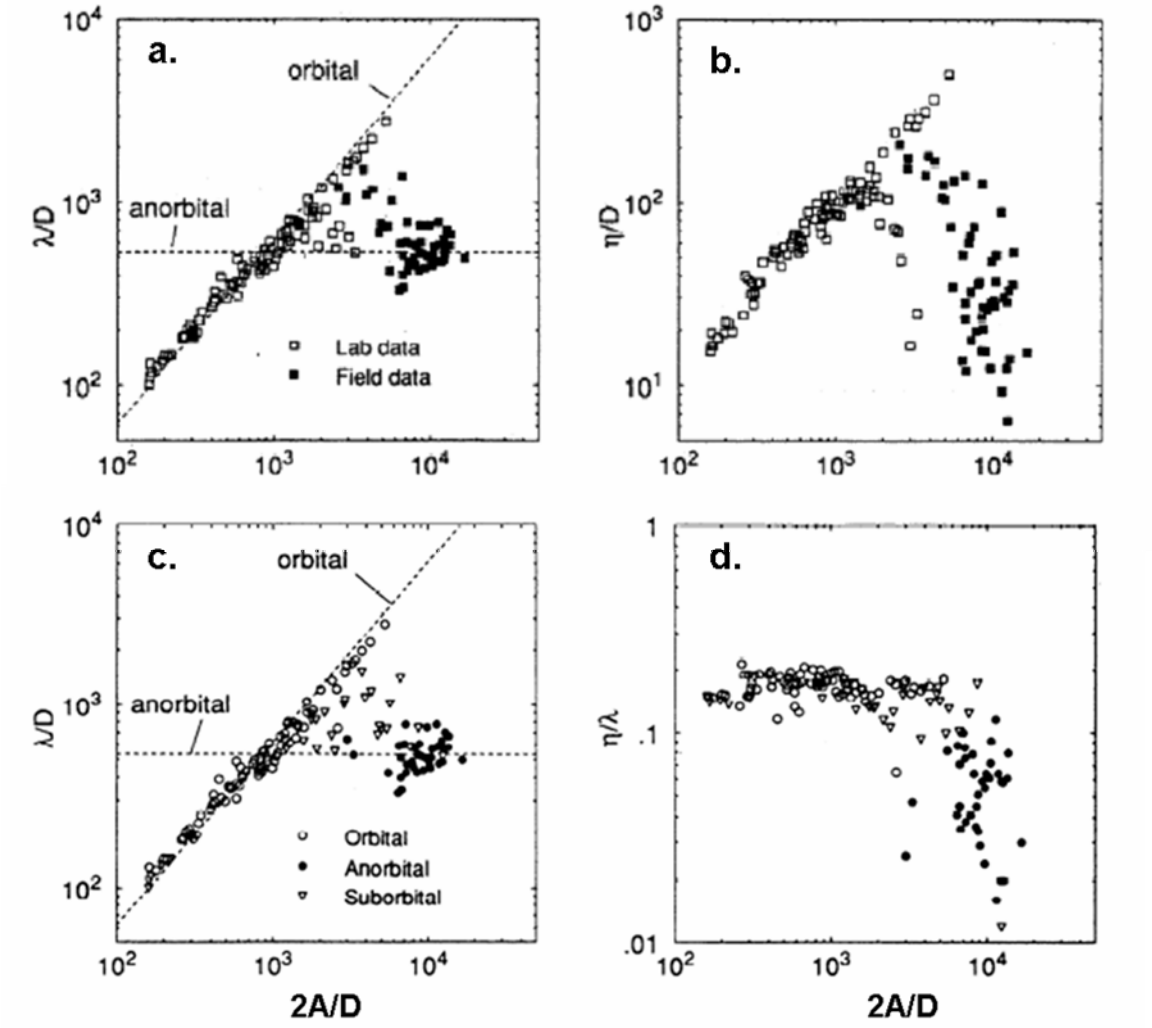

Figure 1.3. Normalized ripple wavelength (a) and normalized ripple height (b) as a function of normalized wave orbital diameter, measured from previous field and laboratory studies. Normalized ripple wavelength (c) and ripple steepness (d) as a function of normalized wave orbital diameter, showing *Wiberg and Harris* [1994] classification of ripples, indicated by symbol type. Dashed lines in (a) and (c) represent observed trends for ripple wavelength of orbital and anorbital ripples. Figure adapted from *Wiberg and Harris* [1994].

Wiberg and Harris [1994] found that most of the orbital ripples were observed in flumes, whereas most of the anorbital ripples were observed in the field. In their study they also examined ripple steepness, defined by the ratio of the ripple height to the ripple wavelength, η/λ.

A method of predicting ripple wavelength and height was constructed by *Wiberg and Harris* [1994]. Assumed known parameters are grain size D, wave period T, and either wave orbital diameter d_o or wave height H and water depth h, which are related by

$$d_o = \frac{H}{\sinh(kh)} \tag{3}$$

The value of kh was computed iteratively using the relationship $k_D h = kh \tanh(kh)$, where $k_D = 4\pi^2/(gT^2)$. The method involves determining the ripple type and then using this information along with the known flow characteristics to compute the ripple dimensions.

In identifying ripple type, *Wiberg and Harris* [1994] determined that the most important difference between orbital and anorbital ripples is the ratio of wave boundary-layer thickness to ripple height, which can be approximated by the ratio d_o/η. For small values of the ratio, the ripples are of the orbital type and at large values of the ratio the ripples are of the anorbital type. Analysis of the data set resulted in expressions for the ripple wavelength and steepness for orbital and anorbital ripples. For orbital ripples

$$\lambda_{orb} = 0.62 d_o \tag{4}$$

$$(\eta/\lambda)_{orb} = 0.17 \tag{5}$$

For anorbital ripples

$$\lambda_{ano} = 535D \tag{6}$$

with data points scattered around this value. Anorbital ripples have a maximum steepness closer to 0.12 [*Wiberg and Harris*, 1994], with ripple steepness decreasing with increasing wave orbital diameter until sheet flow conditions were reached. *Wiberg and Harris* [1994] evaluated their model with previous field and laboratory ripple geometry observations and determined their model to be relatively accurate.

Crawford and Hay [2001] examined the affect of wave orbital velocity skewness on the direction and magnitude of net sediment transport during a 1995 autumn storm event during a field experiment undertaken at Queensland Beach, Nova Scotia. Field observations of linear transition ripple geometry and migration were obtained during both the growth and decay phases of the storm event in 3-4 m water depth, where linear transition ripples are defined as long-crested, low-steepness bedforms of the anorbital ripple type [*Crawford and Hay*, 2001].

The geometry of the bedforms was measured using a high resolution laser-video system. Over a time period of 1.5 hours, they found small variations in the observed ripple wavelengths and heights, with a mean ripple wavelength of 8.5 cm and mean ripple height of 0.3 cm, resulting in a mean steepness of 0.04 [*Crawford and Hay*, 2001]. Figure 1.4 shows their observed linear transition ripples in a parameter space adapted from *Clifton and Dingler's* [1984] classification scheme, using the average ripple wavelength of 8.5 cm and a median grain diameter of 0.0174 cm. In their plot they used the significant wave orbital semi-excursion, *A*, to represent the orbital motion of the wave,

where A is the horizontal distance a water particle will travel during half of a wave period and is defined as two times the wave orbital diameter ($A = 2d_o$) and

$$A = \frac{2u_{rms}}{\omega} \tag{7}$$

and

$$\omega = \frac{2\pi}{T} \tag{8}$$

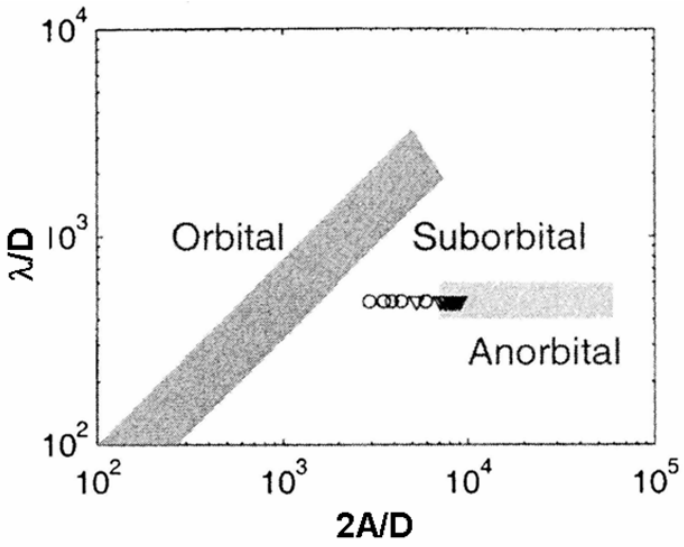

Figure 1.4. Position of *Crawford and Hay's* [2001] observed linear transition ripples in normalized wave orbital diameter-ripple wavelength space. Figure adapted from *Crawford and Hay* [2001].

The ripples observed during their experiment were determined to be of the anorbital type, based on their lack of dependence of ripple wavelength on wave orbital diameter and the large orbital excursion-to-ripple wavelength ratio [*Crawford and Hay*, 2001]. However, their observations of lower wave orbital diameter cases fall into the suborbital range of the previous classification scheme. Therefore, it was concluded that in terms of the ripple wavelength-orbital diameter based classification proposed by *Clifton and Dingler* [1984], the anorbital ripple class extends into a smaller wave orbital diameter range than suggested by the diagram [*Crawford and Hay*, 2001].

Hay and Mudge [2005] further explored *Clifton's* [1976] conceptual model in the SandyDuck97 experiment. They examined the sea-bed response to over a dozen storm events, focusing on two cross-shore locations. In these observations, sea-bed geometry was in response to random waves and mean flow conditions. Their primary purpose was to determine whether bed state is related mainly to second-order (e.g., energy) or third-order (e.g., skewness, *Sk*, or asymmetry, *As*) statistics of the incident wave field [*Hay and Mudge*, 2005]. Comparing the two locations, they were able to investigate the importance of third-order statistics by eliminating several parameters from *Clifton's* [1976] model. Grain size distributions, peak wave periods, and mean values of root-mean-square wave orbital velocity, u_{rms}, were nearly identical for each location, removing them as factors in bed state variability among the locations. By examining bed state occurrences as a function of u_{rms} and wave *Sk* and *As*, (Figure 1.5), *Hay and Mudge* [2005] determined that bed state occurrence should not be based on wave nonlinearity in predictive models, and that u_{rms} is a critical parameter for determining bed state occurrence.

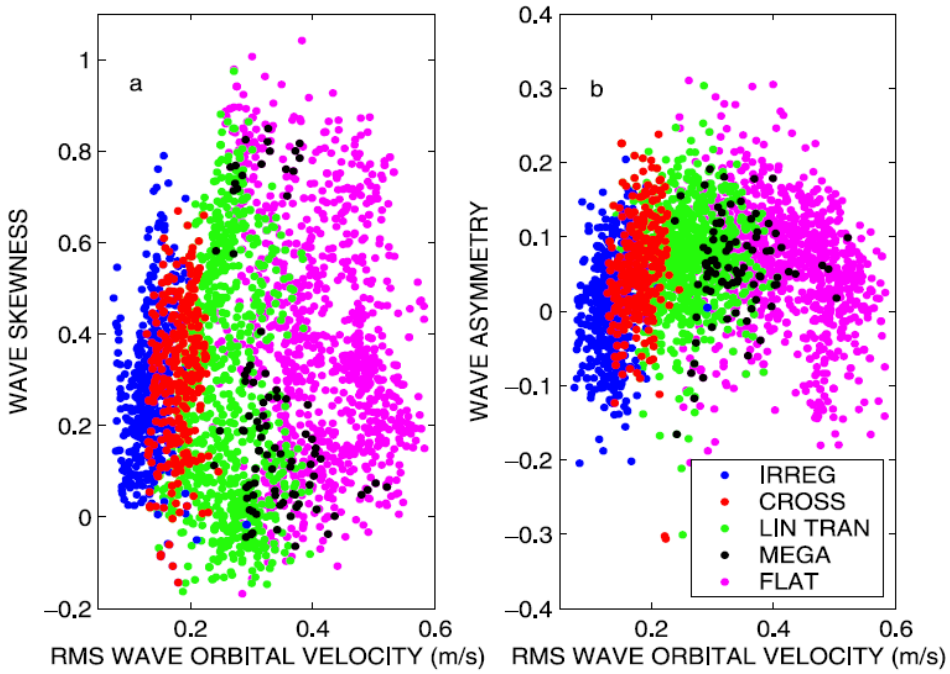

Figure 1.5. Bed state occurrence as a function of root-mean-square wave orbital velocity for wave skewness (a) and wave asymmetry (b). Adapted from *Hay and Mudge* [2005].

CHAPTER 2

OBSERVATIONS

In this investigation, the sea-bed geometry was measured in a large scale wave flume at the O.H. Hinsdale Wave Research Laboratory at Oregon State University. The observations were obtained as part of the multi-institutional, collaborative CROss Shore Sediment Transport EXperiment (CROSSTEX), conducted in summer 2005. The goal of CROSSTEX is to examine sediment transport dynamics in the nearshore, wave-breaking and bottom-boundary layer turbulence and sediment suspension, ripple formation over short timescales, and beach recovery.

This specific investigation, conducted in a large-scale laboratory setting, was based on similar work done in field experiments. The large wave flume is 104 m long, 3.7 m wide and 4.6 m deep. The hydraulic ram, hinged-type wavemaker in the flume is capable of producing oscillatory flows and simulating both regular and random waves. A variety of regular and random wave climates were produced during the investigation, with offshore wave heights, H_{mo}, ranging from 30 to 60 cm and wave periods, T, ranging from 4 to 8 sec.

The flume is narrow and therefore not capable of producing significant alongshore flows (incident waves, low-frequency waves, or mean currents) typically observed in nature. To reduce the tank seiche, the wave runs were generally less than 20 minutes. These limited duration runs also limit the tanks ability to accurately reproduce the cross-shore directed low-frequency waves and mean flow motions generally observed in nature. Consequently the focus of this investigation is on the sea-bed geometry induced by free surface gravity waves in the incident band ($4 < T < 8$ s).

The flume was filled with coarse grained sediment for the experiment, with a median grain diameter, D, of 0.0218 cm. Sediment samples were obtained at several data collection locations throughout the experiment and were sieved to determine the grain size distribution (the sediment analysis can be found in Appendix C).

2.1 Instrumentation

Data used in this work were collected over a period of two months and obtained from instrumentation deployed from a single mast suspended on a movable cart. A photograph of the deployed instrumentation is shown in Figure 2.1. Data were collected at two separate offshore locations, shown in Figure 2.2, both prior to the wave breaking region. The flume was divided into sections, known as Bays, each identified by a number, with Bay 1 being the furthest onshore. Observations made on yeardays 173 to 179 were collected at Station 1, between Bays 13 and 14, approximately 40 m offshore in a water depth of 1.723 m. Data were obtained on yeardays 180 to 197 from Station 2, which was located more onshore at Bay 9, approximately 30 m offshore in a water depth of 1.625 m.

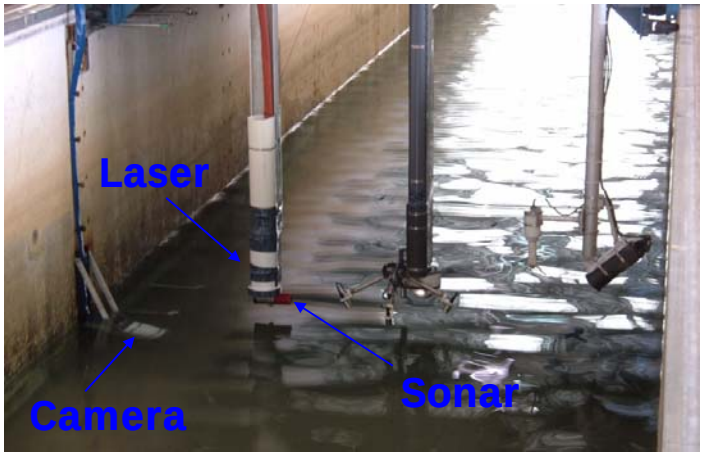

Figure 2.1. Photograph of instrument deployment at CROSSTEX.

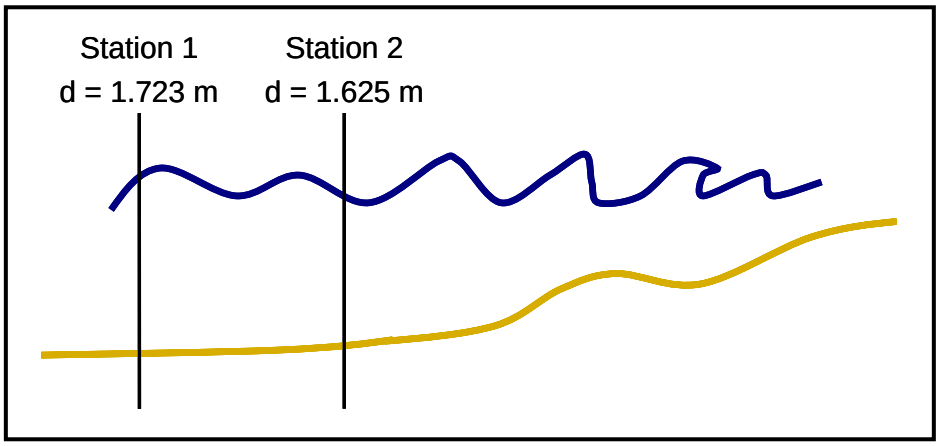

Figure 2.2. Sketch of data collection locations (not to scale).

A Dantec Particle Image Velocimetry (PIV) system was administered to observe the sea-bed evolution resulting from wave generations. The completely submersible PIV system consisted of a downward pointing 120 mJ Nd:Yag laser located 1 m above the bed, illuminating a vertical slice of the water column. The laser was paired with an obliquely oriented 1 mega-pixel digital camera attached to the flume wall, which collected images at 15 Hz of generally a 22 cm x 22 cm area of the bed. The reflection of the laser on the sea-bed allowed the camera to record the bed evolution as a result of the waves produced. Both the laser and the camera were housed in underwater pressure cases and could communicate remotely with a control unit onshore, which recorded and stored the data and images collected.

The three components of velocity at a single location were measured using a Sontek Acoustic Doppler Velocimeter (ADV) current meter. The ADV current meter was sampled at 25 Hz and was located 30 cm above the bed; it was mounted on the same mast as the PIV laser and IMAGENEX sonar. Data from the ADV current meter was collected using Sontek HorizonADV software and was processed to determine wave orbital velocities in the cross shore direction.

2.2 Ripple Geometry Measurements

Ripple geometry measurements were taken manually from PIV images collected near the end of each wave simulation (Figure 2.3). Coordinates of ripple crests and troughs were obtained manually and used to calculate ripple wavelengths, λ, and heights, η, using simple geometry and algebra; bed slope was accounted for in all calculations. The bedforms observed during the experiment were of various profiles, some being

complex and difficult to interpret. Figure 2.3b is an example of an ambiguous ripple formation; sea-bed images that showed several ripple crests and troughs, such as Figure 2.3b, were measured and averaged to determine the ripple geometry for that particular wave generation. In the case of a flat bed occurrence, such as in Figure 2.3c, ripple height was taken to be zero and ripple wavelength was given a value much greater than the size of the image frame.

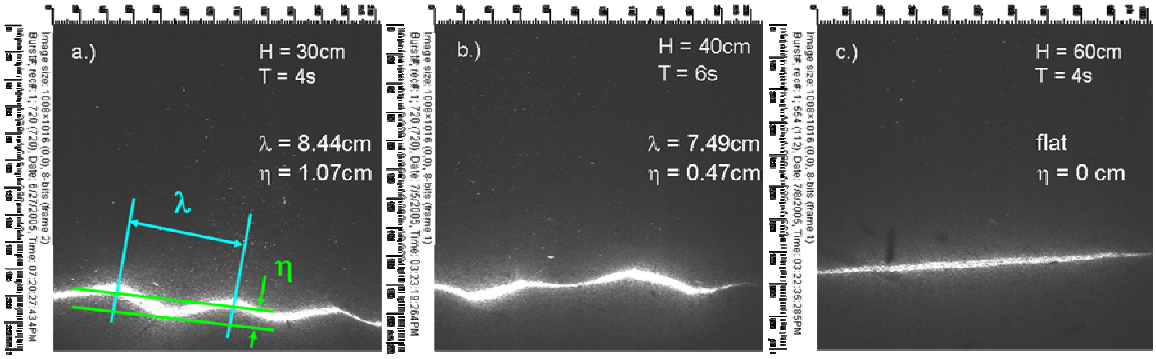

Figure 2.3. PIV images demonstrating regular ripple formations (a), irregular ripple formations (b), and a completely flat bed (c).

CHAPTER 3

RESULTS

3.1 Hydrodynamic Conditions

Values of the root-mean-square velocity, u_{rms}, were determined from the three-dimensional fluid velocities measured with the ADV current meter at a single free-stream location. The root-mean-square velocities were used to calculate significant wave orbital velocity, u_o, defined by $u_o=2u_{rms}$ [*Thorton and Guza*, 1983].

A variety of wave climates were simulated during the experiment. An increase in the offshore wave height, H_{mo}, resulted in an increase in the root-mean-square wave orbital velocity, u_{rms}, as shown in Figure 3.1a and 3.1b. Not surprisingly, this dependent relationship was observed at both stations. A flat bed, shown by the solid symbols, is induced more often for greater H_{mo}. At Station 1 (Figure 3.1a), the random waves created with a narrower-banded TMA spectrum, with γ=10 (blue), had higher u_{rms} values than the waves created with a broader-banded TMA spectrum with γ=20 (green). However, the TMA γ=20 (green) waves induced a flat bed at lower u_{rms} values than the TMA γ=10 (blue) waves that were generated. At Station 2 (Figure 3.1b), the monochromatic (red) waves had higher u_{rms} values than the TMA γ=10 (blue) waves. For an H_{mo} of 30cm, the

monochromatic (red) waves did result in a flat bed, unlike the random waves, however there was only one such occurrence.

Figure 3.1 also shows the relationship between the offshore wave height, H_{mo}, and the significant wave orbital semi-excursion, A, for Station 1 (c) and Station 2 (d). An increase in H_{mo} caused an increase in A at both water depths, where $2A=d_o=\frac{u_o T}{\pi}$. This figure also illustrates how higher period waves have higher significant wave orbital semi-excursions. Linear regressions for the different wave periods are shown in Figure 3.1 for H_{mo} vs. A; these trend lines demonstrate that A increases more abruptly with longer wave periods. However, for the observations from Station 1, the linear regression for the 8s waves is less abrupt due to the inclusion of both the TMA γ=10 and TMA γ=20 waves in the same regression.

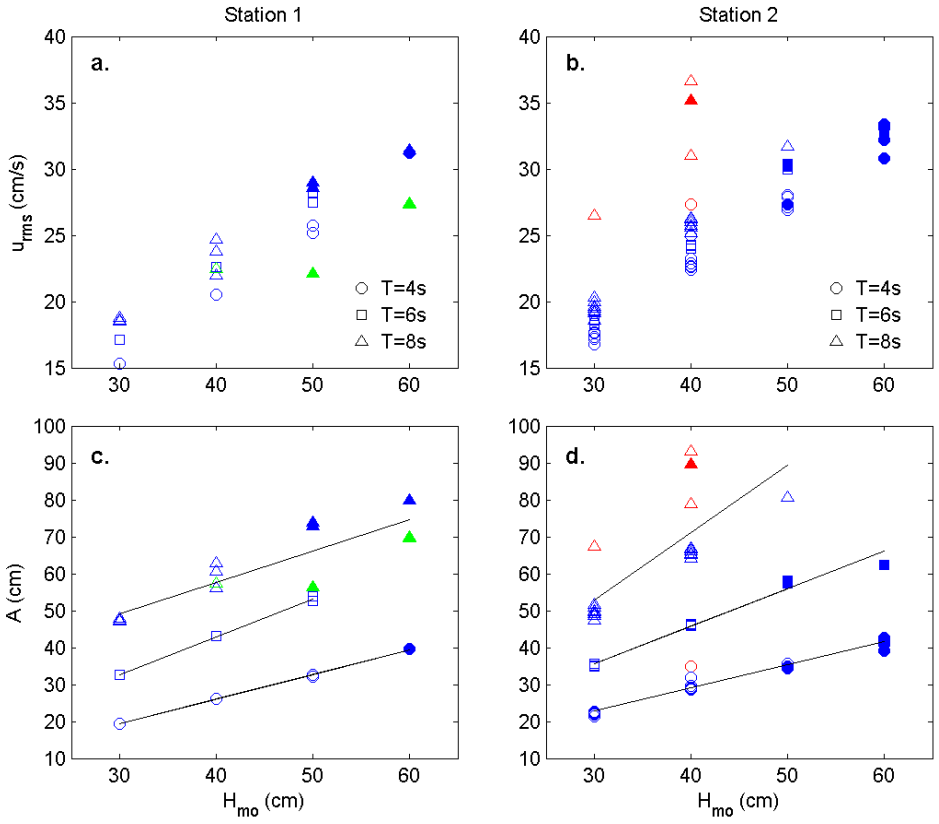

Figure 3.1. Relation of offshore wave height to the root-mean-square wave orbital velocity for Station 1 (a) and Station 2 (b) and to significant wave orbital semi-excursion for Station 1 (c) and Station 2 (d). Blue symbols represent waves generated using the TMA spectrum with γ=10, green symbols represent waves generated using the TMA spectrum with γ=20, red symbols represent monochromatic waves. Solid symbols indicate a flat bed and open symbols indicate a rippled bed.

3.2 Ripple Geometry

Numerous diverse ripple formations were observed throughout the experiment. The classification of bed state occurrences in the experiment is limited to rippled and flat bed states only, at the present time. The PIV images used to analyze the bedforms express the ripple formations in only two-dimensions (x-z), and therefore the long shore

characteristics of the ripples are unknown. In this investigation, bedforms with ripple heights less than 0.2 cm ($\eta < 0.2$ cm) were considered flat. In cases where the bedform was completely flat in the PIV image, the ripple wavelength, λ, was given an extreme value to distinguish it from rippled beds.

3.2.1 Ripple Wavelength

According to *Clifton* [1976], the bedforms observed could be classified into four main fields. The field of symmetric bedforms was examined by considering the relations of ripple wavelength, λ, to wave orbital diameter, d_o, and grain size diameter, D. Figure 3.2 displays these relationships and will be used in comparison with the classifications of *Clifton and Dingler* [1984] to determine specific symmetric ripple types formed throughout the study. A D value of 0.0218 cm was used for all analyses, and the orbital motion of the wave is characterized by the significant wave orbital semi-excursion, where $2A=d_o$. Also shown in Figure 3.2 is the ripple classification scheme of *Wiberg and Harris* [1994]. Orbital ripples are indicated by the equation $\lambda=0.62d_o$, representing the proportionality of ripple spacing to wave orbital diameter. The range of anorbital ripple types is shown by the equation $\lambda=535D$, which represents the dependence of ripple spacing on grain size as determined by *Wiberg and Harris* [1994].

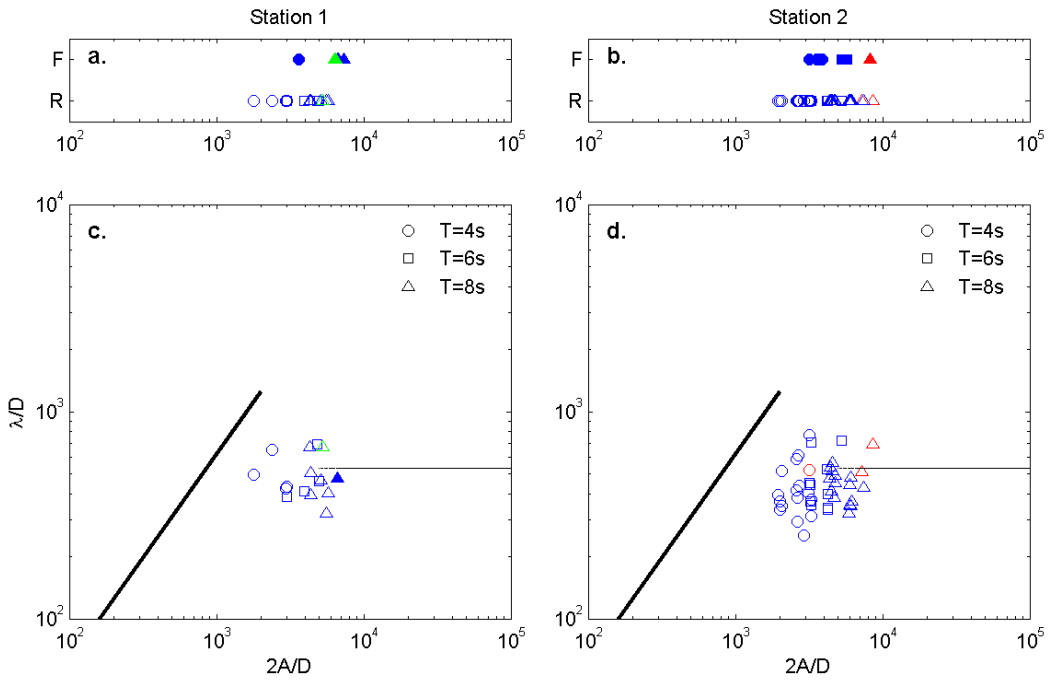

Figure 3.2. Normalized ripple wavelength as a function of normalized wave orbital diameter for Station 1 (c) and Station 2 (d). Bed state occurrences shown for Station 1 (a) and Station 2 (b), where F represents flat bed and R represents rippled bed. Blue symbols represent waves generated using the TMA spectrum with γ=10, green symbols represent waves generated using the TMA spectrum with γ=20, red symbols represent monochromatic waves. Solid symbols indicate a flat bed and open symbols indicate a rippled bed.

According to *Clifton and Dingler* [1984] and *Wiberg and Harris* [1994], the bedforms observed during the experiment would be of the suborbital and anorbital type at both water depths. According to *Crawford and Hay* [2001], the ripples would be of the anorbital type defined by their large wave orbital semi-excursion to ripple wavelength ratios. There were no occurrences of orbital ripples, shown by the dependence of ripple spacing on grain size for all data points. At Station 1 (Figure 3.2c), the data points have $2A/D$ values in the range of 1700 to 7400 and λ/D values in the range of 300 to 700, with

the exception of the flat bed data which is outside the axes limits of this figure. The data points with $2A/D$ values greater than 5000 would be considered anorbital ripples according to *Clifton and Dingler* [1984]. According to *Clifton and Dingler* [1984], anorbital ripples have λ/D values of 400 to 600; however several of the observed bedforms with $2A/D$ values greater than 5000 have λ/D values less than 400. Figure 3.2a shows that at Station 1, flat beds occurred at higher wave orbital diameter values than the rippled beds for the various wave periods.

At the more onshore location, Station 2 (Figure 3.2d), the data had $2A/D$ values in the range of 1900 to 8600 and λ/D values in the range of 250 to 780, excluding the flat bed occurrences, which are not in the axes limits of this figure. The cluster of data points for the wide range of $2A/D$ values suggest that ripple spacing did not depend on wave orbital diameter. At Station 2 (Figure 3.2b), there were several instances when flat beds occurred for the same values of A as when rippled beds occurred for the various wave periods. This also indicates that ripple spacing was independent of wave orbital diameter.

Examining the relations of the bedforms developed compared to the wave conditions produced, suggests different results for the ripple classifications than indicated by the *Clifton and Dingler* [1984] classification scheme. A dimensionalized form of the *Clifton and Dingler* [1984] classification is shown in Figure 3.3 and the division between suborbital and anorbital ripple types is shown by the shaded areas, where the left side of the figure is the suborbital range and the right side is the anorbital range. These ranges were determined based on *Clifton and Dingler's* [1984] findings where anorbital ripples

occur for 2*A*/*D* values greater than or equal to 5000. Using a *D* value of approximately 0.02 cm, anorbital ripples are shown to occur when *A* equals 50.

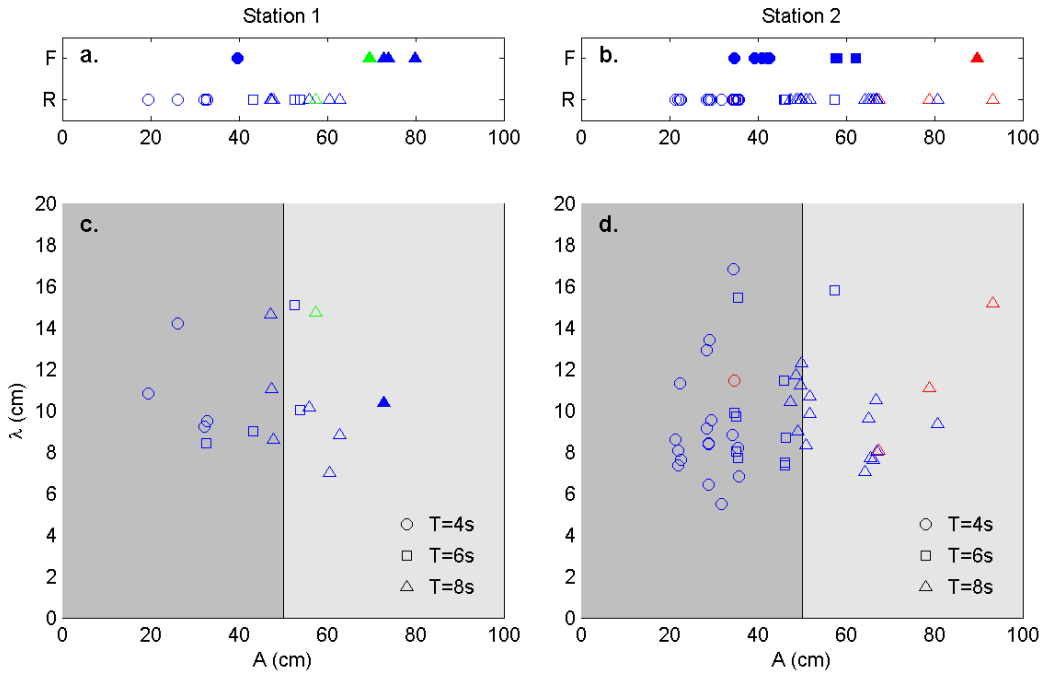

Figure 3.3. Relationship of the ripple wavelength to the significant wave orbital semi-excursion for Station 1 (c) and Station 2 (d). Bed state occurrences shown for Station 1 (a) and Station 2 (b), where F represents flat bed and R represents rippled bed. Blue symbols represent waves generated using the TMA spectrum with γ=10, green symbols represent waves generated using the TMA spectrum with γ=20, red symbols represent monochromatic waves. Solid symbols indicate a flat bed and open symbols indicate a rippled bed.

The classifications of *Clifton and Dingler* [1984] shown by the shaded regions in Figure 3.3, indicate both suborbital and anorbital ripples were observed at both Station 1 (c) and Station 2 (d). A limited number of ripples observed have wavelengths larger than

approximately 12 cm. These bedforms are either high offshore wave height cases (i.e. H_{mo}=50 to 60 cm) where the bed is flattening, or irregular ripples where the PIV plane is near a termination point of the ripple crest. By examining the PIV images throughout the wave generation during these particular runs, the irregular wave cases were identified. Examples of anomalous data includes yd 175 Run 02, where A=57.3 cm/s and λ=14.75 cm, and yd 182 Run 02, where A=35.5 cm/s and λ=15.43 cm. Images of these bedforms are included in Appendix A and are indicated as irregular in Table B.1 in Appendix B.

Disregarding the anomalous data, it was determined that only anorbital ripples were observed at both stations. These findings are in disagreement with the classification of *Clifton and Dingler* [1984], but are consistent with *Crawford and Hay* [2001]. For both stations there appears to be no dependency of ripple spacing on the wave orbital semiexcursion. At Station 1 (Figure 3.3c) λ ranges from 7 to 15 cm for all values of A and at Station 2 (Figure 3.3d) λ ranges from 5 to 16 cm for all values of A. This suggests that purely anorbital ripples occurred at both water depths. Average ripple wavelengths of 9.85 cm at Station 1 and 9.25 cm at Station 2 were calculated. Looking at the bed state occurrences (Figure 3.3a and 3.3c), it is seen that for a given wave period, flat beds occurred at higher values of A than rippled beds.

The relation of ripple wavelength to u_{rms} was also investigated (Figure 3.4). No dominant trends are seen in the ripple wavelength for increasing u_{rms}. There is a slight tendency for λ to decrease with increasing u_{rms} for 8s period waves. At both stations, flat beds occurred at higher values of u_{rms} than rippled beds (Figure 3.4a and 3.4b).

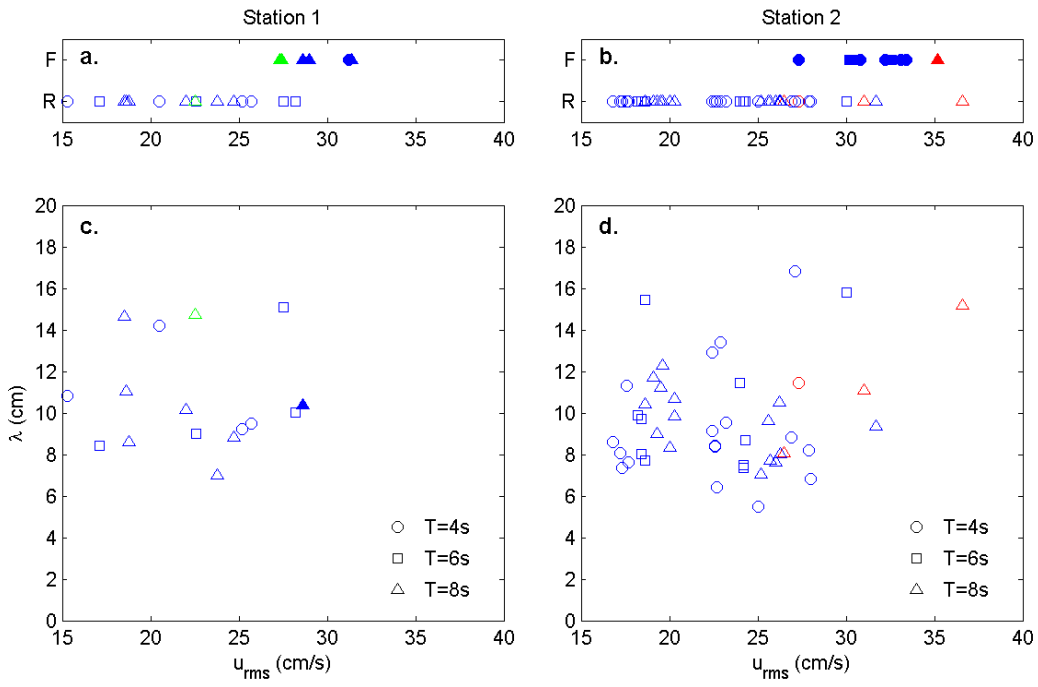

Figure 3.4. Relationship of the root-mean-square wave orbital velocity to ripple spacing for Station 1 (c) and Station 2 (d). Bed state occurrences shown for Station 1 (a) and Station 2 (b), where F represents flat bed and R represents rippled bed. Blue symbols represent waves generated using the TMA spectrum with γ=10, green symbols represent waves generated using the TMA spectrum with γ=20, red symbols represent monochromatic waves. Solid symbols indicate a flat bed and open symbols indicate a rippled bed.

3.2.2 Ripple Height

The findings of *Wiberg and Harris* [1994] indicate that the parameter that best explains the differences between primary ripple types is the ratio of near-bed wave orbital diameter to ripple height. This is examined in Figure 3.5 for the data collected during this experiment. The data from Station 1 (Figure 3.5c) shows ripple height decreases with increasing wave orbital diameter until a flat bed is induced, consistent with *Wiberg and Harris* [1994]. Data from Station 2 (Figure 3.5d) is clustered about a range of η values

for the higher 2*A*/*D* values. *Wiberg and Harris* [1994] concluded that higher d_o/η ratios indicate anorbital ripples; this is particularly apparent at Station 2 (Figure 3.5d), where the data points occur at high 2*A*/*D* values and the η values are clustered in the same range for all 2*A*/*D* values.

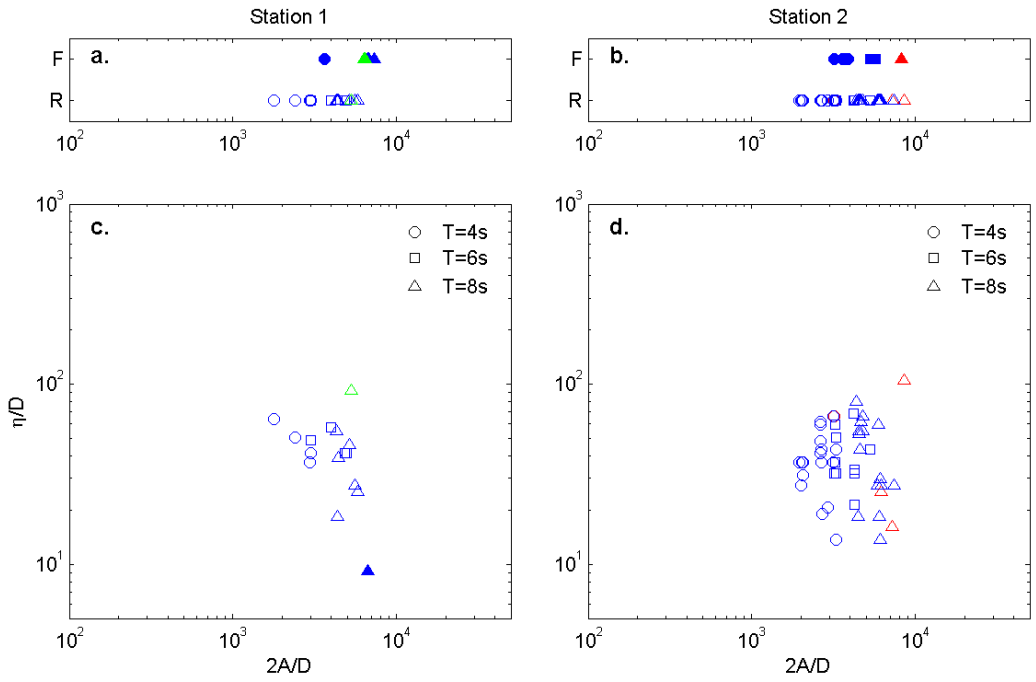

Figure 3.5. Normalized ripple height as a function of normalized wave orbital diameter for Station 1 (c) and Station 2 (d). Bed state occurrences shown for Station 1 (a) and Station 2 (b), where F represents flat bed and R represents rippled bed. Blue symbols represent waves generated using the TMA spectrum with γ=10, green symbols represent waves generated using the TMA spectrum with γ=20, red symbols represent monochromatic waves. Solid symbols indicate a flat bed and open symbols indicate a rippled bed.

The relation of ripple height to significant wave orbital semi-excursion was also examined (Figure 3.6) for both water depths. For any particular wave period, ripple height decreases with increasing *A*, up until a flat bed is induced; this was observed at both Stations. There are erratic data points at both stations where the bedform had a significant ripple height for a large wave orbital diameter. Inspecting the PIV image used in determining these ripple heights it was seen that these ripples were highly irregular and are not indicative of the majority of sea-bed responses for that particular wave generation. Critical limits where a flat bed is induced are apparent at both Stations, with shorter period waves inducing a flat bed sooner. At Station 1 (Figure 3.6a), 4s period waves induce a flat bed at values of *A* greater than 40 cm and 8s period waves induce a flat bed at values of *A* greater than approximately 67 cm. At the shallower water depth, Station 2 (Figure 3.6b), flat beds were induced at values of *A* greater than 35, 57, and 90 cm for 4, 6, and 8s wave periods respectively. Data from Station 2 (Figure 3.6b) for each wave period is slightly aligned in vertical bands, where some rippled beds occur at equal values of *A* as flat beds. This suggests that *A* is not a reasonable indicator for determining critical limits for flat beds because it is a function of the wave period.

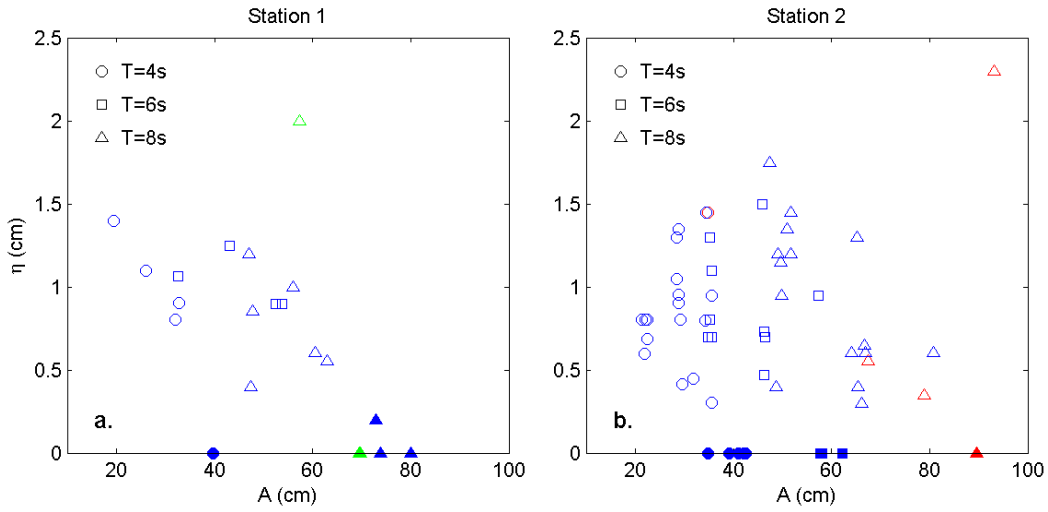

Figure 3.6. Relationship of the ripple height to the significant wave orbital semi-excursion for Station 1 (c) and Station 2 (d). Bed state occurrences shown for Station 1 (a) and Station 2 (b), where F represents flat bed and R represents rippled bed. Blue symbols represent waves generated using the TMA spectrum with γ=10, green symbols represent waves generated using the TMA spectrum with γ=20, red symbols represent monochromatic waves. Solid symbols indicate a flat bed and open symbols indicate a rippled bed.

Similar trends were seen in the relation of ripple height, η, to u_{rms} at both water depths, shown in Figure 3.7. It is encouraging to see that ripple height decreases with increasing u_{rms} according to wave period, with flat beds occurring at the highest values of u_{rms}. Critical limits for inducing a flat bed according to u_{rms} are apparent at Station 1 (Figure 3.7c) and Station 2 (Figure 3.7d), with rippled bed occurrences having lower u_{rms} values. Considering u_{rms} for determining limits for flat bed occurrences appears to be more reasonable than A, because of the more apparent trends with wave period.

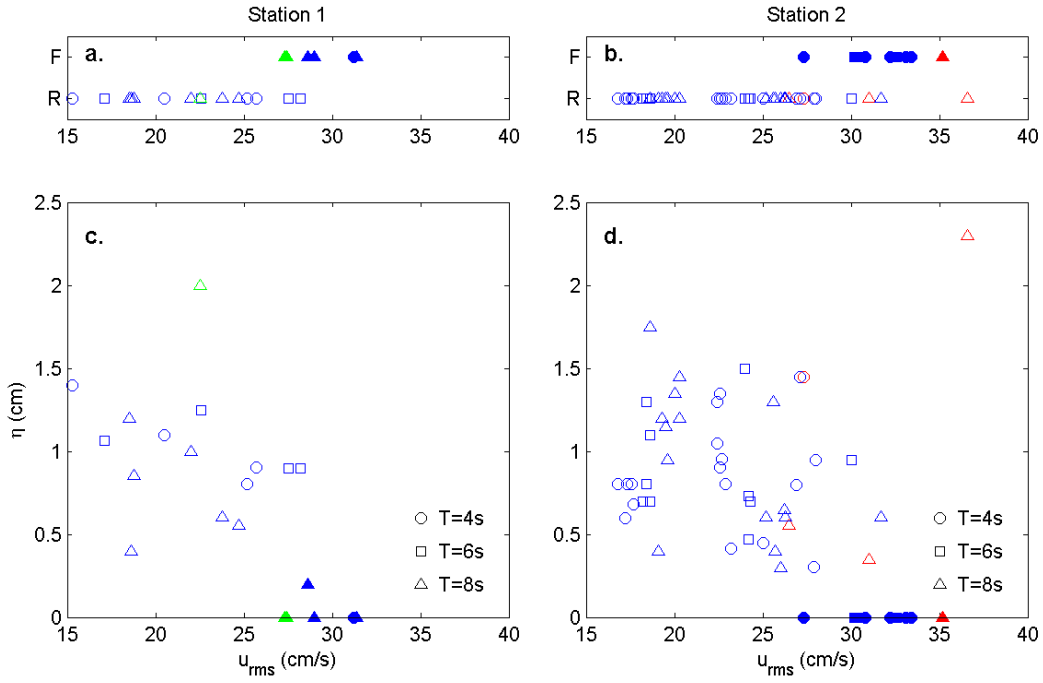

Figure 3.7. Relationship of the root-mean-square wave orbital velocity to ripple height for Station 1 (c) and Station 2 (d). Bed state occurrences shown for Station 1 (a) and Station 2 (b), where F represents flat bed and R represents rippled bed. Blue symbols represent waves generated using the TMA spectrum with γ=10, green symbols represent waves generated using the TMA spectrum with γ=20, red symbols represent monochromatic waves. Solid symbols indicate a flat bed and open symbols indicate a rippled bed.

3.2.3 Ripple Steepness

The ripple geometry resulting from a range of wave conditions represented numerous different profiles, with various combinations of ripple heights and ripple wavelengths being produced. Examining the steepness of the ripples allows for both ripple geometry parameters to be analyzed. Similar to the classification shown by *Wiberg*

and Harris [1994], the relation of ripple steepness, defined by η/λ, to the wave orbital diameter non-dimensionalized by median grain diameter was examined (Figure 3.8).

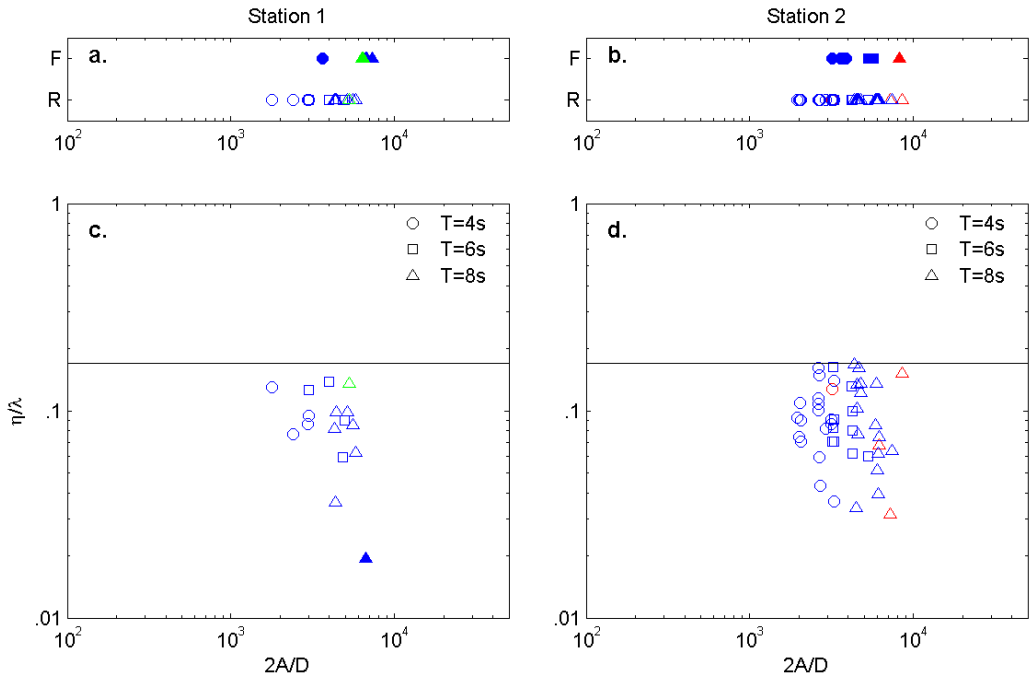

Figure 3.8. Normalized ripple steepness as a function of normalized wave orbital diameter for Station 1 (c) and Station 2 (d). Bed state occurrences shown for Station 1 (a) and Station 2 (b), where F represents flat bed and R represents rippled bed. Blue symbols represent waves generated using the TMA spectrum with γ=10, green symbols represent waves generated using the TMA spectrum with γ=20, red symbols represent monochromatic waves. Solid symbols indicate a flat bed and open symbols indicate a rippled bed.

According to *Wiberg and Harris* [1994], orbital ripples are characterized by a constant steepness of 0.17; anorbital ripples have smaller values of maximum steepness smaller and steepness decreases with increasing orbital diameter. The range of orbital

ripples is shown in Figure 3.8 by the line representing $\eta/\lambda=0.17$. The bedforms observed at both water depths were outside of the orbital ripple range. At Station 1 (Figure3.8c) it is seen that ripple steepness decreases with increasing wave orbital diameter, consistent with *Wiberg and Harris* [1994]. Similar to the results seen in comparisons of ripple wavelength with *A*, measurements of ripple steepness at Station 2 are clustered about a small range of $2A/D$.

A closer investigation was made into the relation of ripple steepness to wave orbital diameter by looking at a dimensionalized relationship (Figure 3.9). At Station 1 (Figure 3.9a) for any particular wave period, the ripple steepness decreases with increasing *A* until a flat bed occurs. At Station 2 (Figure 3.9b) however, there is less of a dependency of ripple steepness on *A*. At the shallower water depth, the data shows slight decreases in ripple steepness with increasing *A* however the data points are more aligned in vertical bands according to wave period. Ripple steepness ranges from the division of the orbital range, $\eta/\lambda=0.17$, all the way to flat bed occurrences for distinct bands of *A* according to wave period. This indicates the ripples at Station 2 are purely anorbital given their independence on wave orbital diameter.

Ripple steepness was also examined as a function of u_{rms} for both water depths (Figure 3.10). It is seen that at both stations, ripple steepness decreases with increasing u_{rms} for a given wave period, as expected based on the relations of ripple height and wavelength to u_{rms}. Again, u_{rms} is a better indicator of flat bed occurrences than *A*.

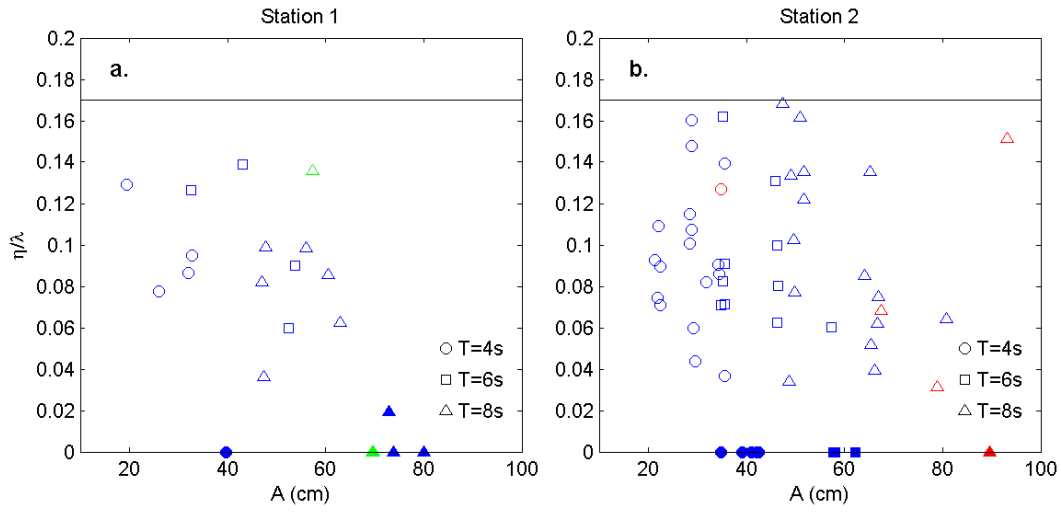

Figure 3.9. Relationship of the ripple steepness to the significant wave orbital semi-excursion for Station 1 (a) and Station 2 (b). Blue symbols represent waves generated using the TMA spectrum with γ=10, green symbols represent waves generated using the TMA spectrum with γ=20, red symbols represent monochromatic waves. Solid symbols indicate a flat bed and open symbols indicate a rippled bed.

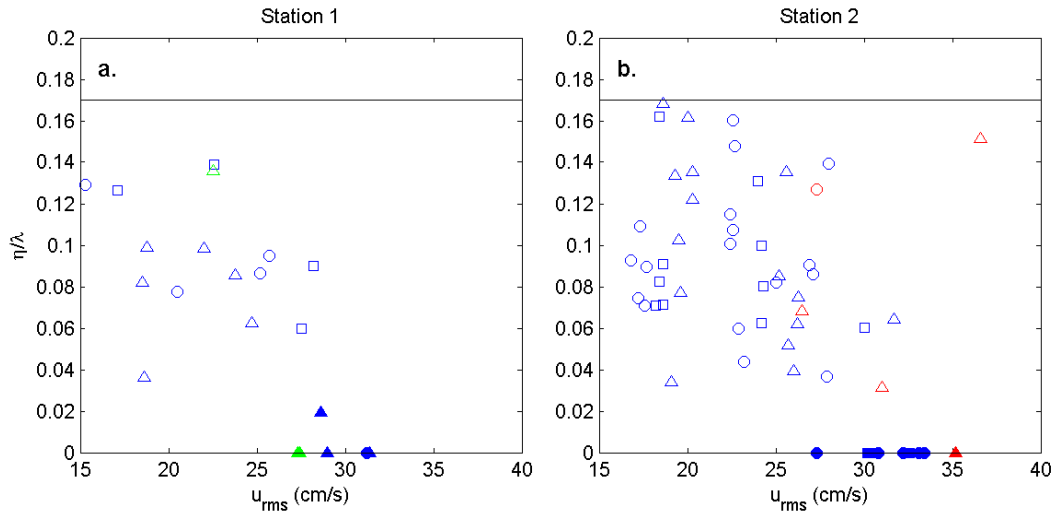

Figure 3.10. Relationship of the root-mean-square wave orbital velocity to ripple steepness for Station 1 (a) and Station 2 (b).

CHAPTER 4

CONCLUSIONS

Observations of the sea-bed response to non-breaking waves have been obtained for a variety of wave conditions. Data was collected during a collaborative, large-scale laboratory experiment, CROSSTEX. Observations were taken in the large wave flume at the O.H. Hinsdale Wave Research Laboratory from two locations of differing water depths, both outside of the wave breaking region. Ripple geometry measurements were manually estimated from PIV images of bedforms created under a variety of wave climates. The occurrences of two bed states, rippled and flat beds, were evaluated during this investigation. A limitation of the PIV images restricted the ripple geometry estimates to two-dimensional ripples. Flat beds were considered to have ripple heights less than 0.2 cm. Bedforms with ripple wavelengths larger than12 cm were determined to be cases where the bed was flattening, or irregular ripples where the PIV plane was near the termination point of the ripple crest.

The hydrodynamic conditions produced during this investigation encompassed a wide variety of wave climates ($30 < H_{mo} < 60$ cm; $4 < T < 8$s), including random waves typically observed in nature. An increase in offshore wave height, H_{mo}, resulted in an

increase in both root-mean-square wave orbital velocity, u_{rms}, and significant wave orbital semi-excursion, A, for both water depths. Broad-banded waves created with the TMA spectrum with γ=20 resulted in lower u_{rms} values than the narrow-banded waves created with the TMA spectrum with γ=10. The broad-band waves also induced a flat bed sooner than the TMA γ=10 waves. Monochromatic waves had the highest values of u_{rms} for a given offshore wave height.

The ripple classification scheme adopted from *Clifton and Dingler* [1984], incorporating the findings of *Wiberg and Harris* [1994], was the basis for classifying the ripples observed during CROSSTEX, however some discrepancies were found. The bedforms observed at both water depths were determined to be of the anorbital type based on the lack of dependence of ripple wavelength on wave orbital diameter. Average ripple wavelengths of 9.85 and 9.25 cm were observed at Stations 1 and 2, respectively. The relation of wave orbital diameter to ripple wavelength normalized by median grain diameter show that the anorbital ripple type extends farther into a smaller range of wave orbital diameters than indicated by the classification scheme of *Clifton and Dingler* [1984], but is consistent with the findings of *Crawford and Hay* [2001].

Trends in the normalized ripple height and steepness as a function of wave orbital diameter were consistent with *Wiberg and Harris* [1994] for Station 1. At Station 2, the data points were clustered in the higher range of wave orbital diameters, indicating anorbital ripples. The tendency for ripple height to decrease with increasing u_{rms} and A for a given wave period was observed at both water depths, with flat beds occurring at the highest values of u_{rms} and A. Also, by comparing the relations of the ripple geometry to

both u_{rms} and A, it would appear that u_{rms} is a better indicator for classifying ripples and determining critical limits where a flat bed will occur. Trends in ripple geometry with A were less distinct, due to the dependence of A on wave period. This result is comparable to the conclusions of *Hay and Mudge* [2005], which indicate that u_{rms} is a critical parameter in determining bed state.

Overall, the findings of this investigation are consistent with those of *Crawford and Hay* [2001] and are comparable to the current ripple classification scheme. Additional investigation into the effect of wave period and water depth on the sea-bed response to non-breaking waves could provide further insight into sedimentary structures in the nearshore. Results from this full scale laboratory investigation can be used to predict morphological evolution in the nearshore zone.

APPENDIX A

PIV OBSERVATIONS

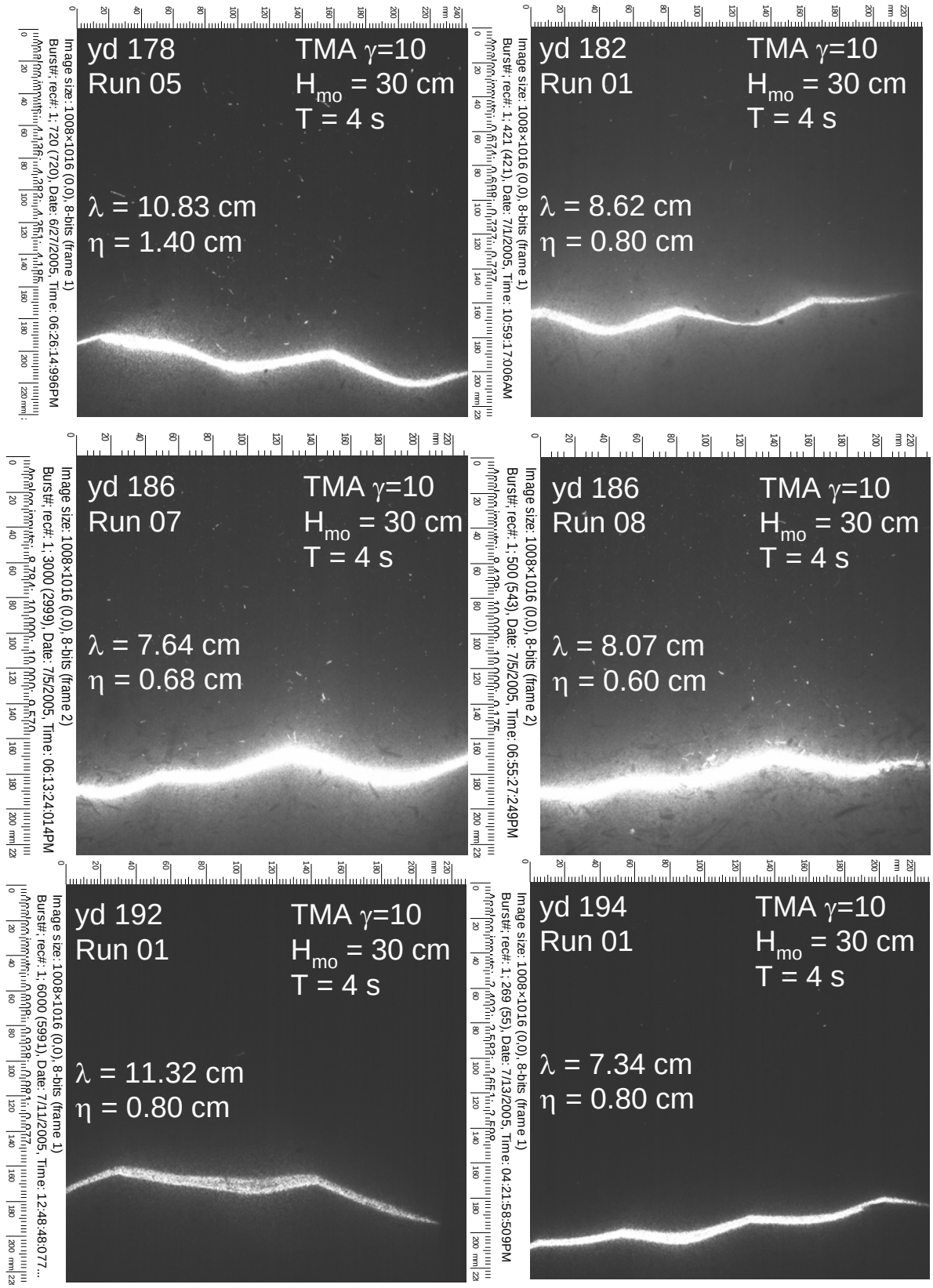

Figure A.1. PIV observations for H_{mo} = 30cm, T = 4s

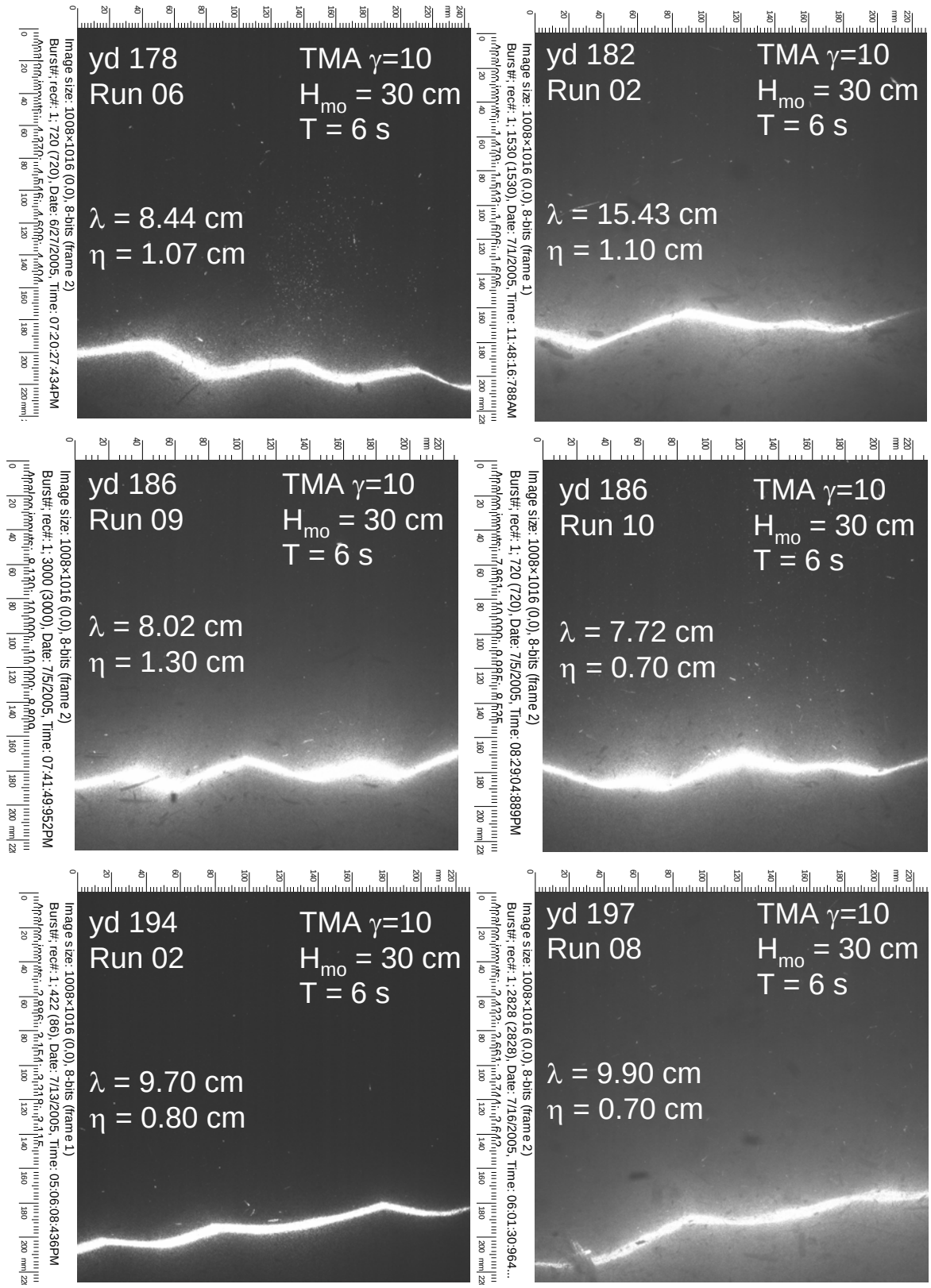

Figure A.2. PIV observations for H_{mo} = 30cm, T = 6s

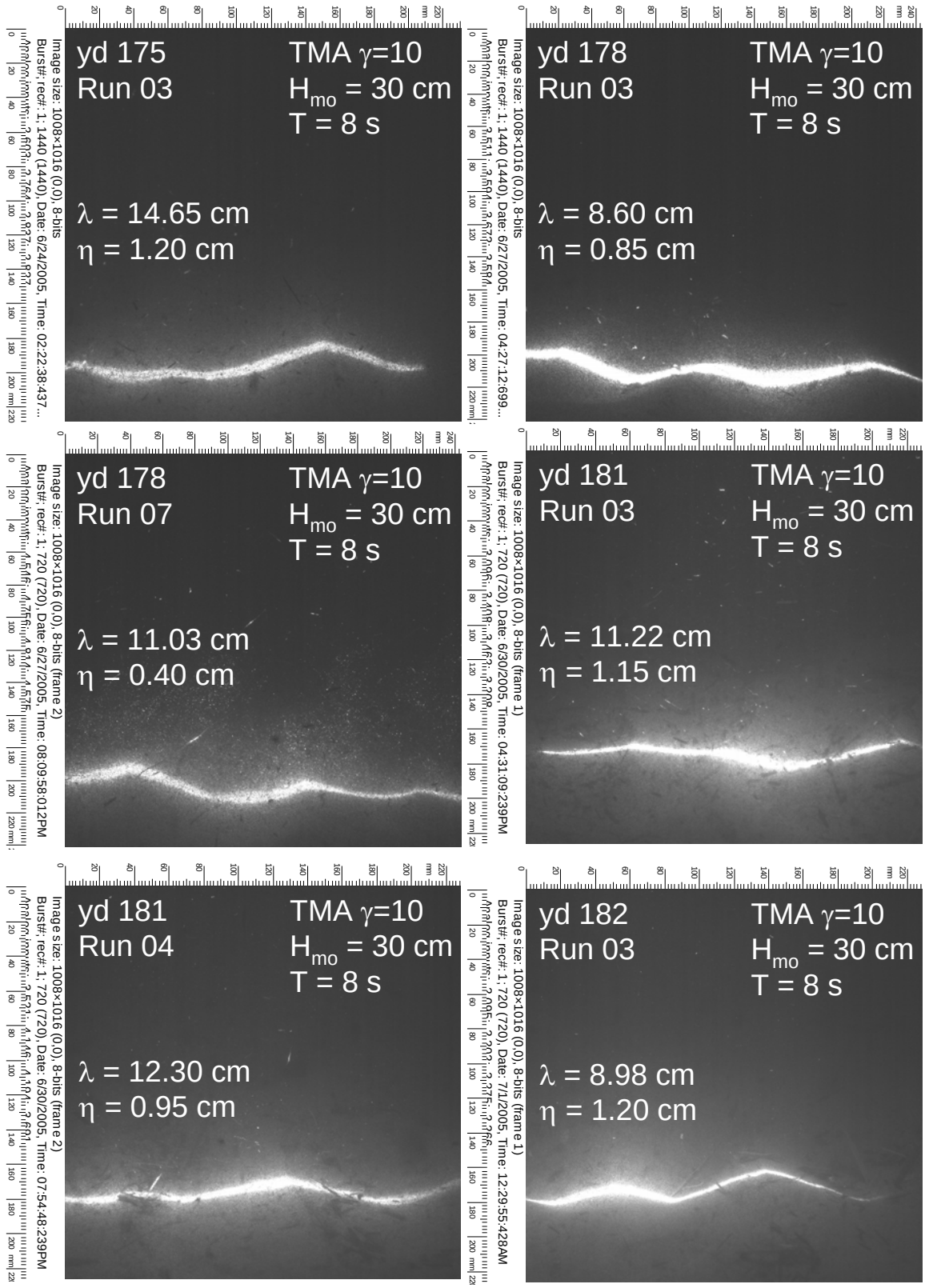

Figure A.3. PIV observations for H_{mo} = 30cm, T = 8s

Figure A.3. continued

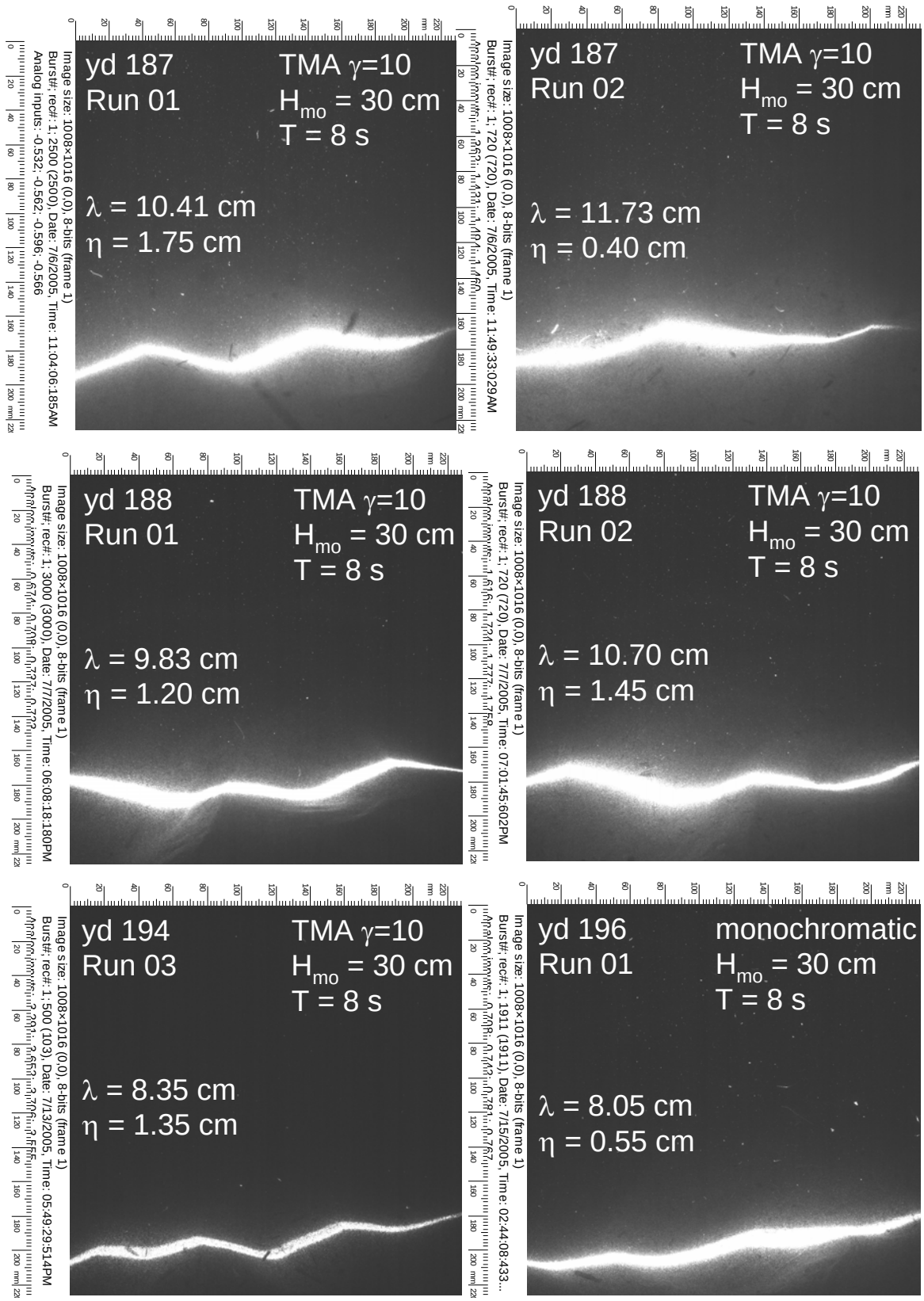

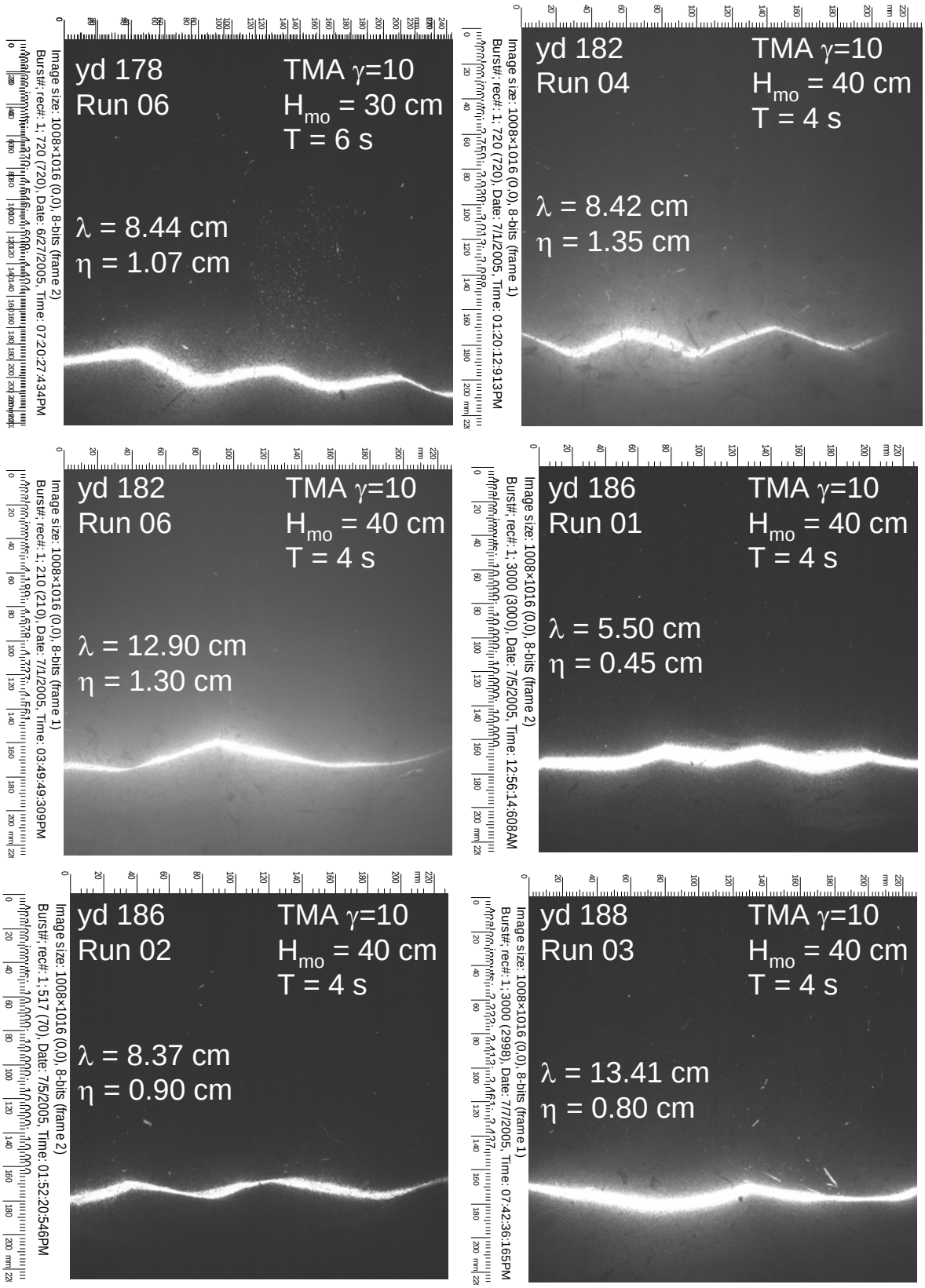

Figure A.4. PIV observations for H_{mo} = 40cm, T = 4s

Figure A.4. continued

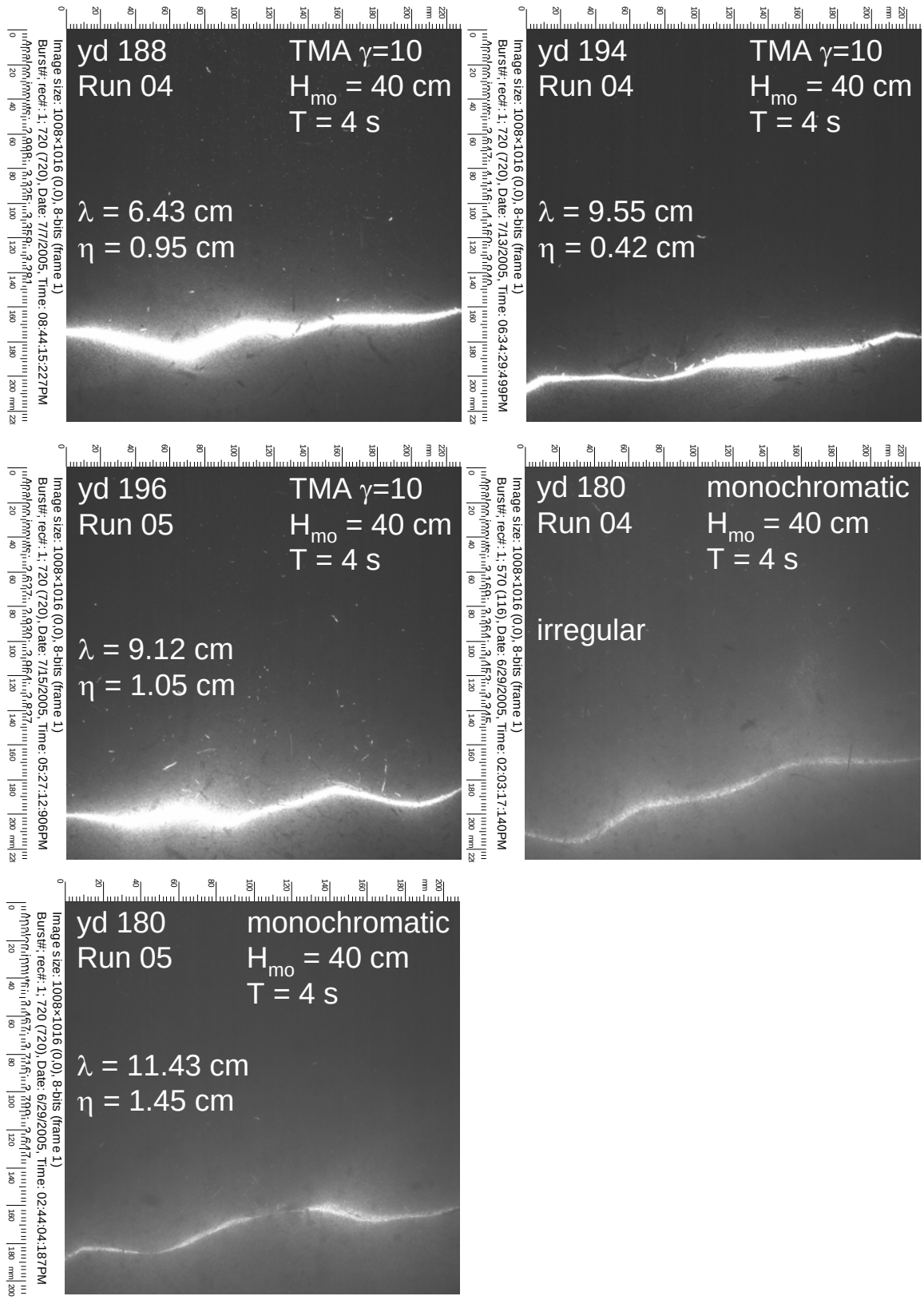

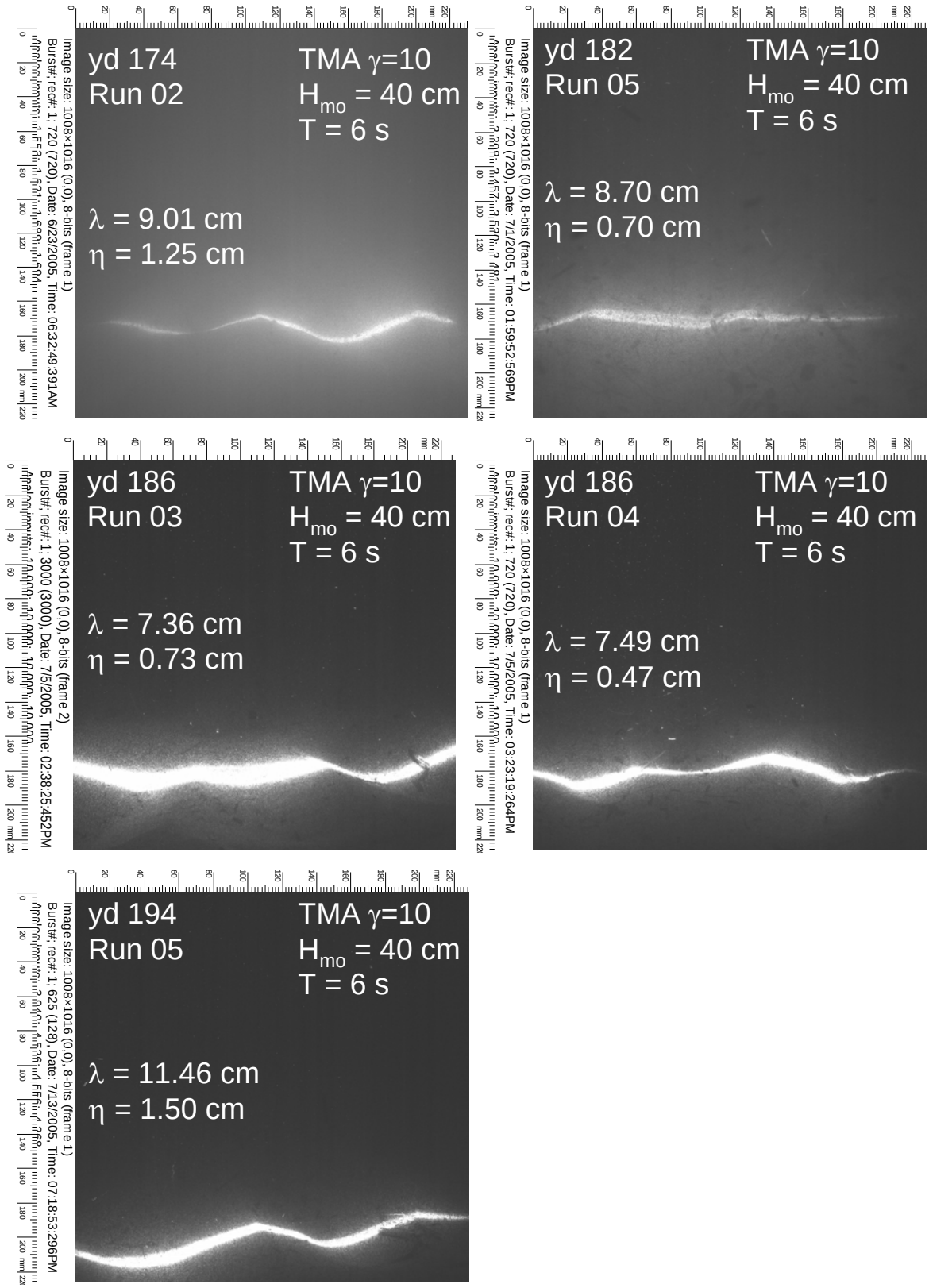

Figure A.5. PIV observations for H_{mo} = 40cm, T = 6s

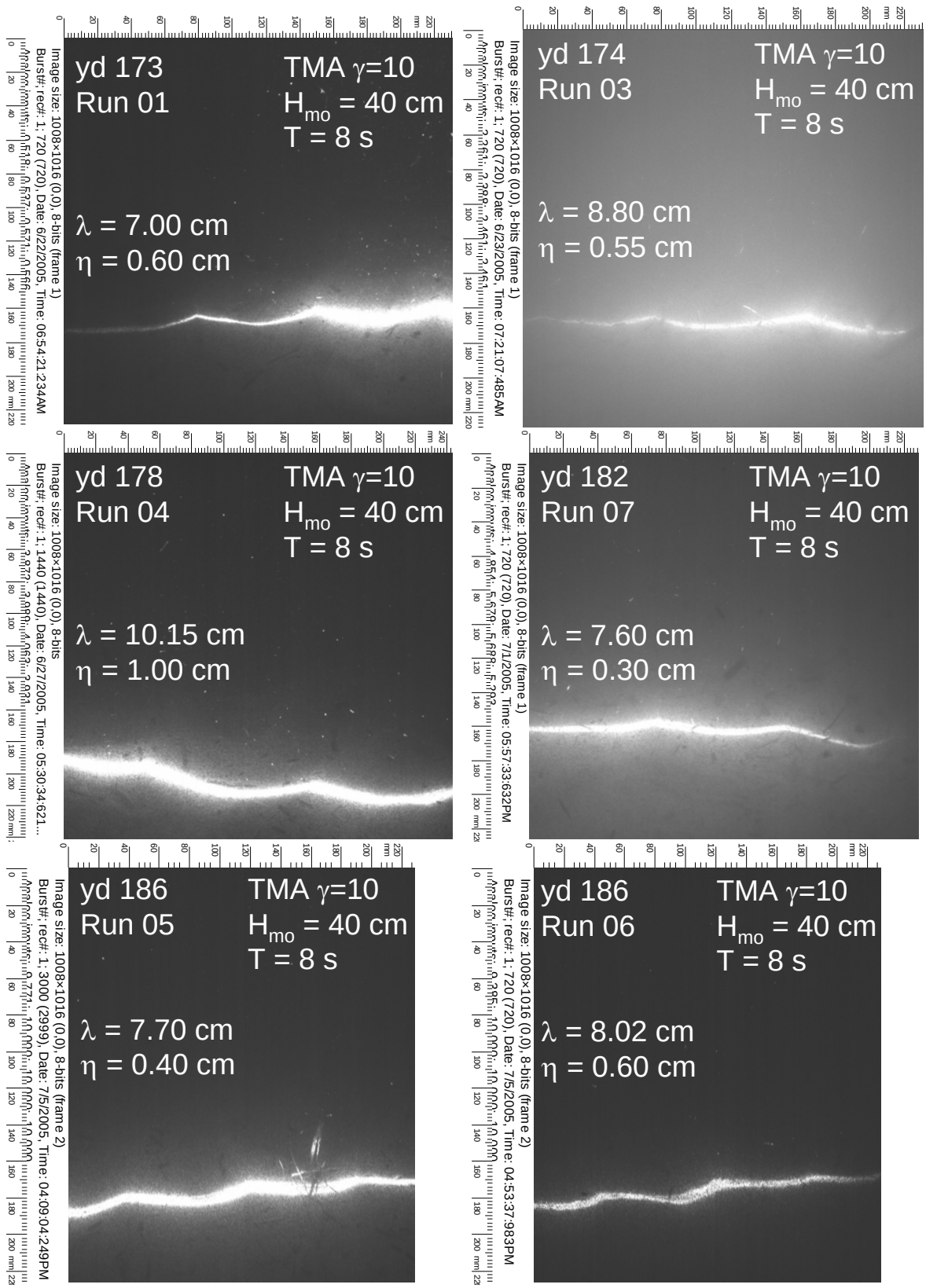

Figure A.6. PIV observations for H_{mo} = 40cm, T = 8s

Figure A.6. continued

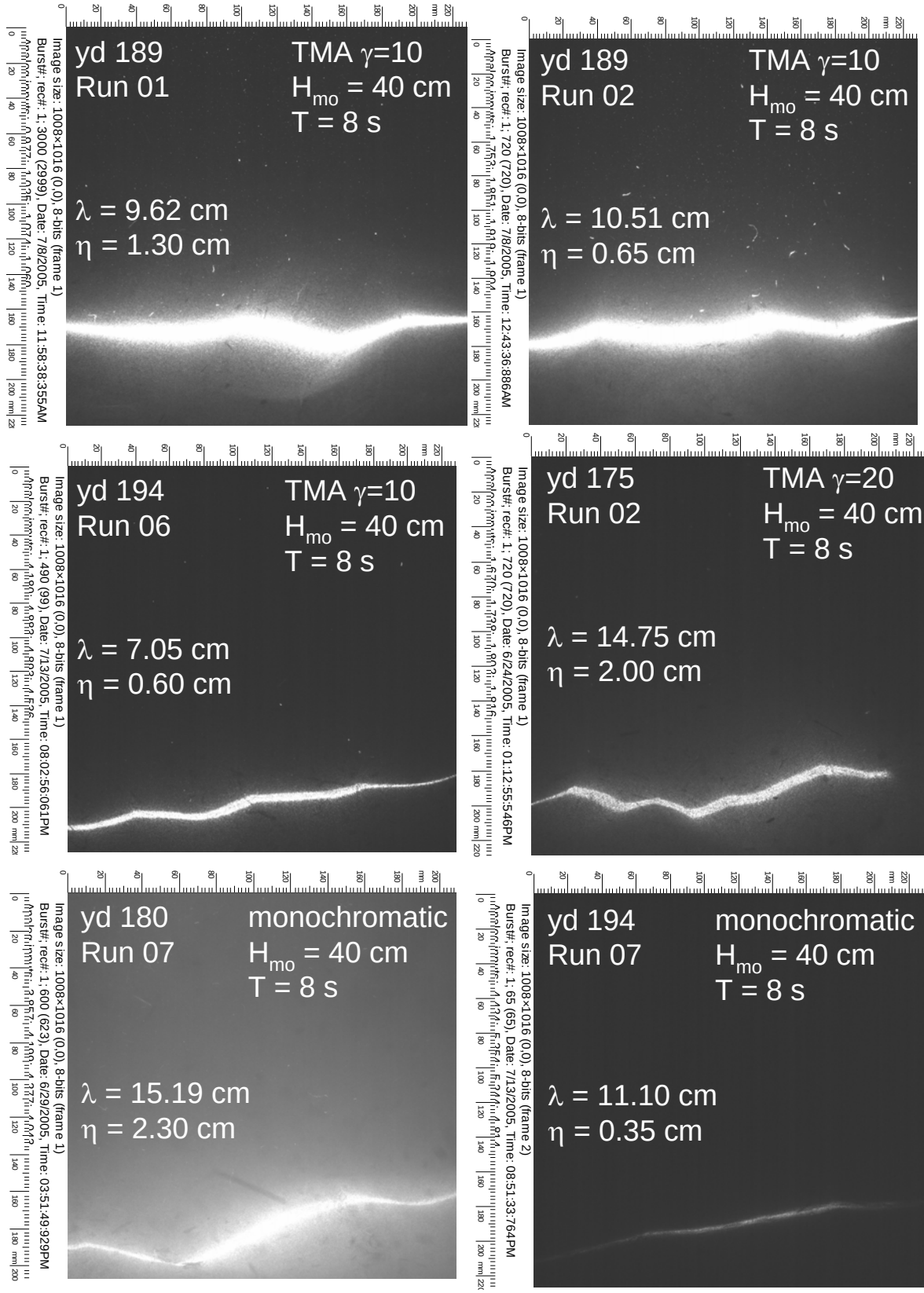

Figure A.6. continued

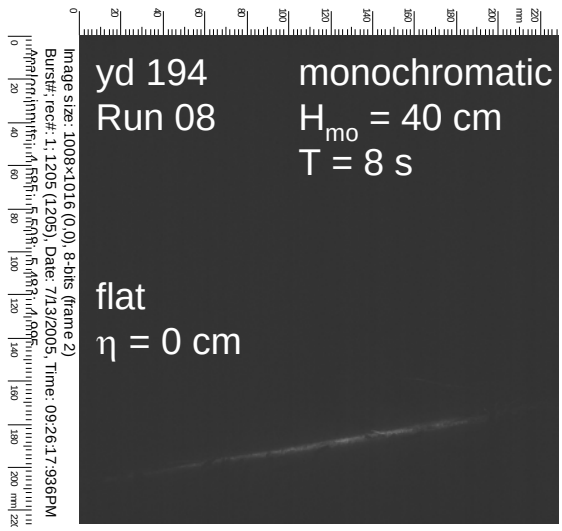

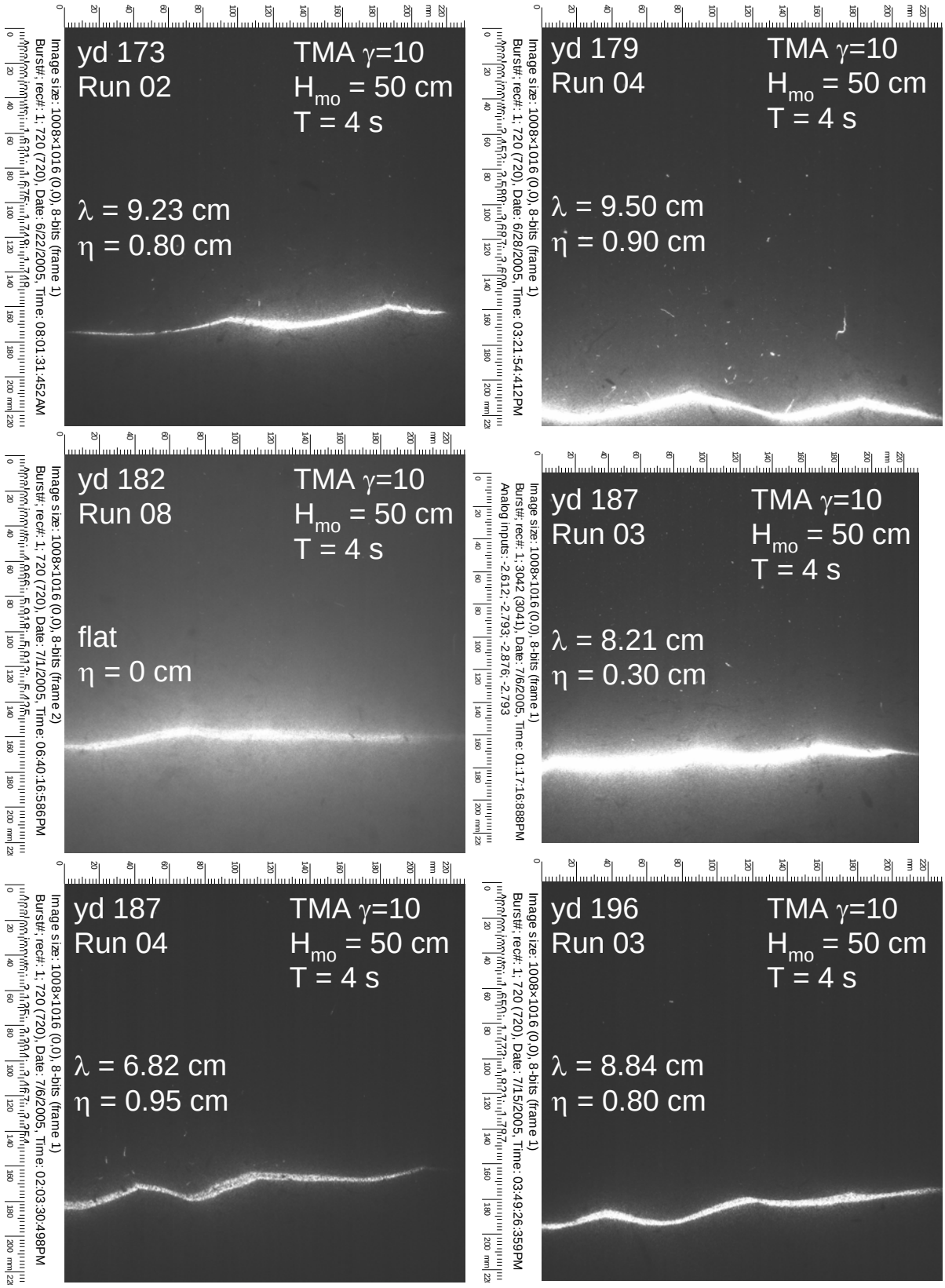

Figure A.7. PIV observations for H_{mo} = 50cm, T = 4s

Figure A.7. continued

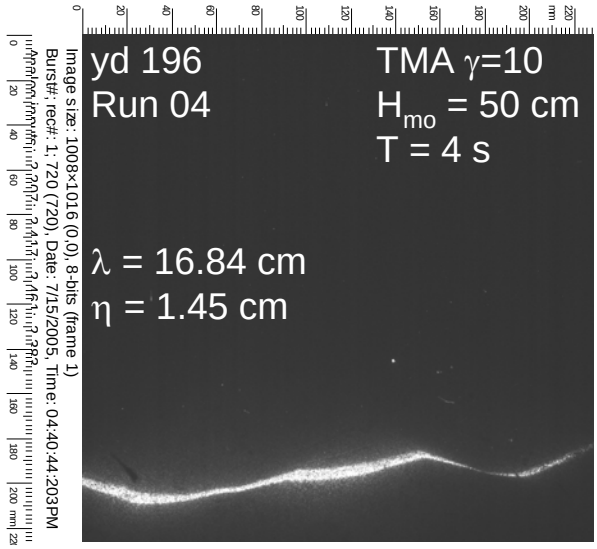

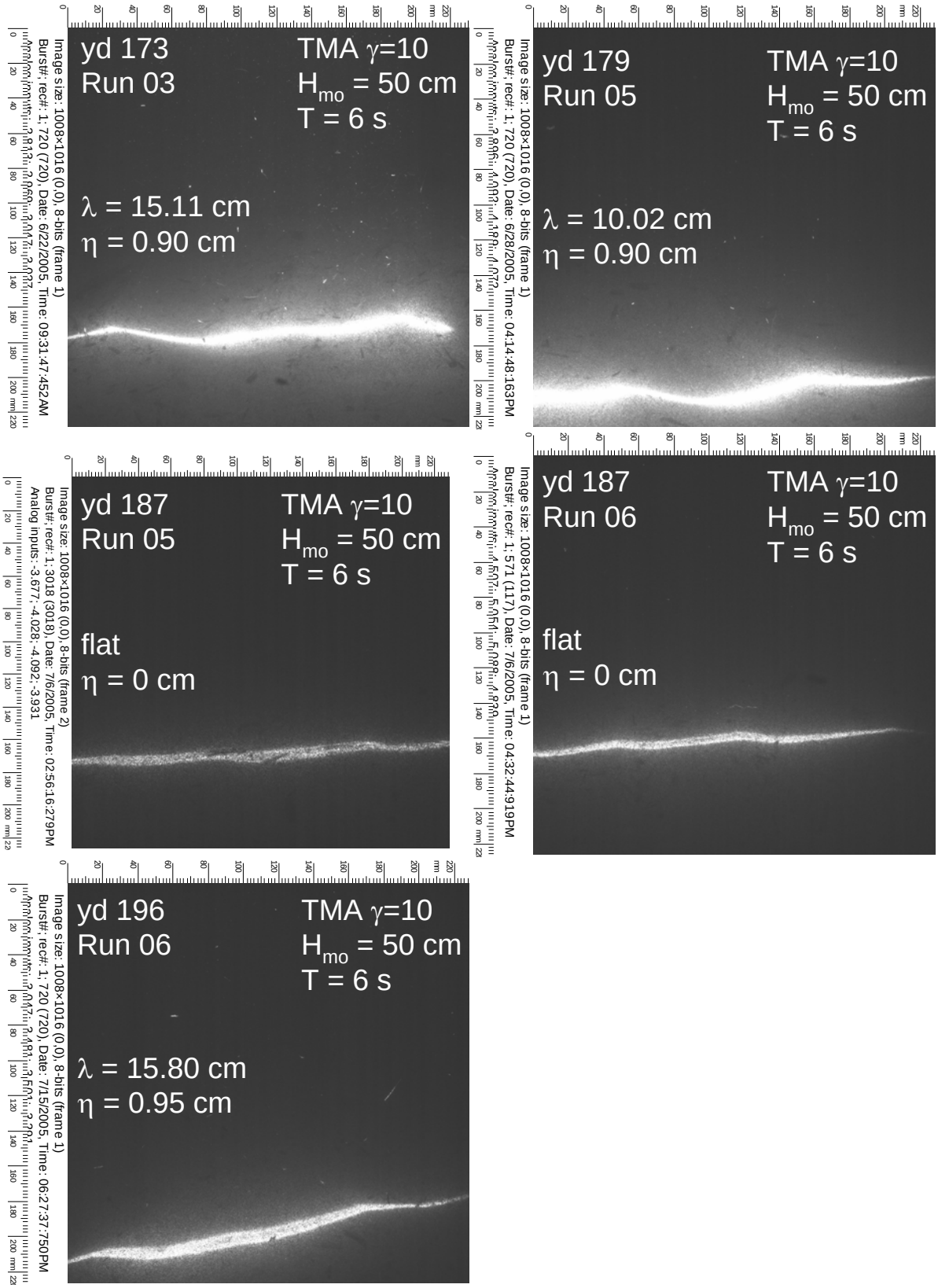

Figure A.8. PIV observations for H_{mo} = 50cm, T = 6s

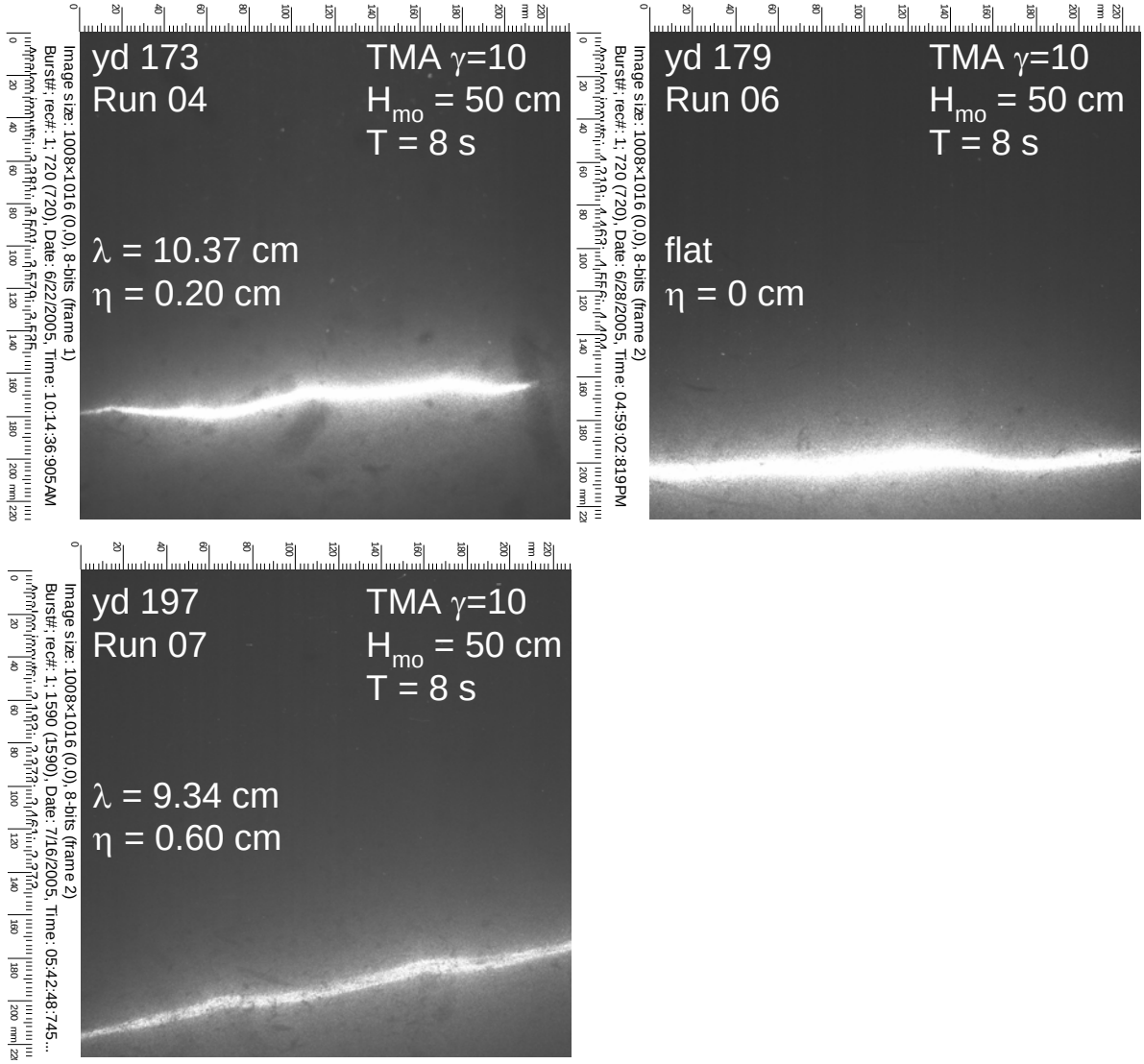

Figure A.9. PIV observations for H_{mo} = 50cm, T = 8s

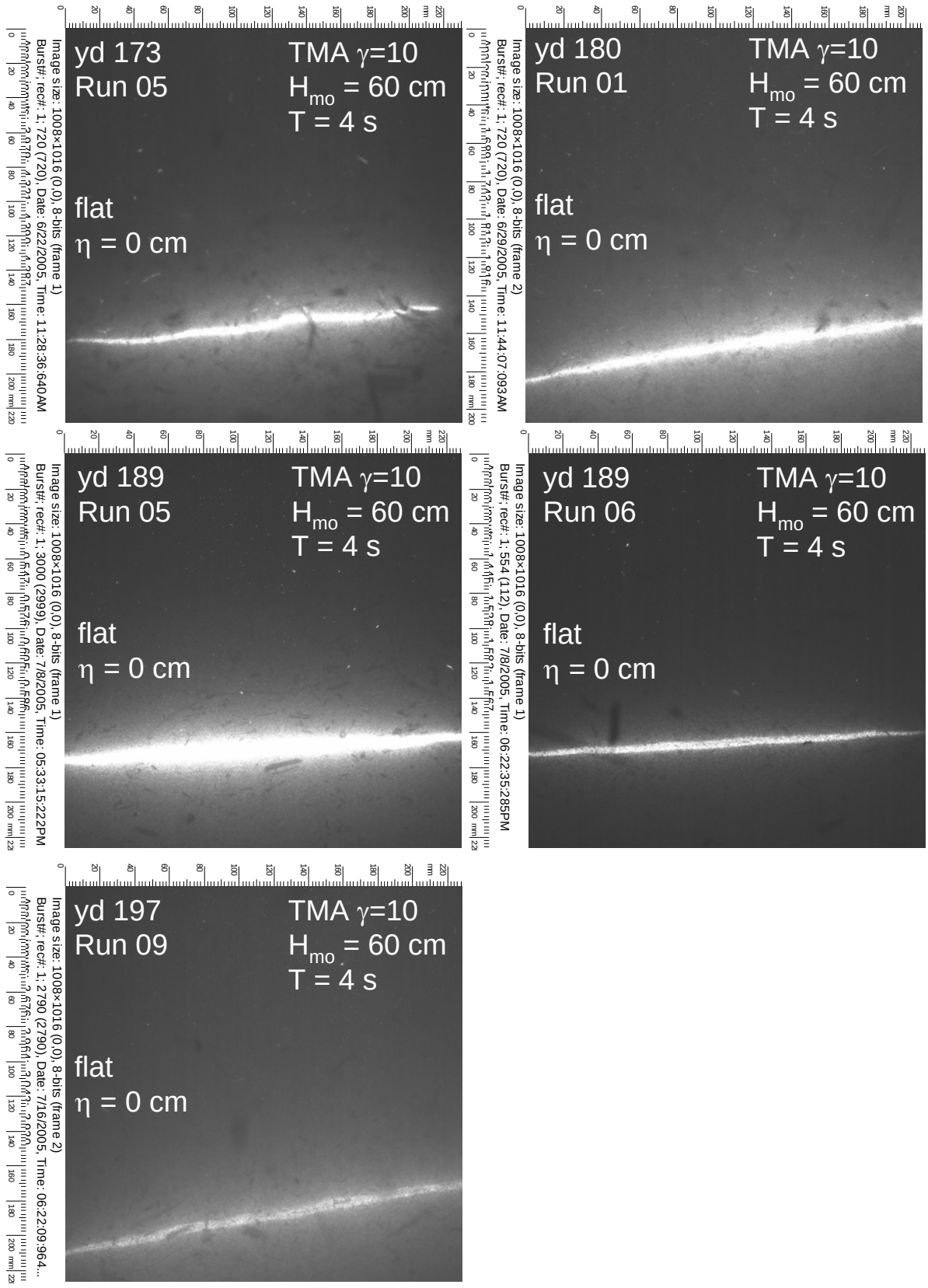

Figure A.10. PIV observations for H_{mo} = 60cm, T = 4s

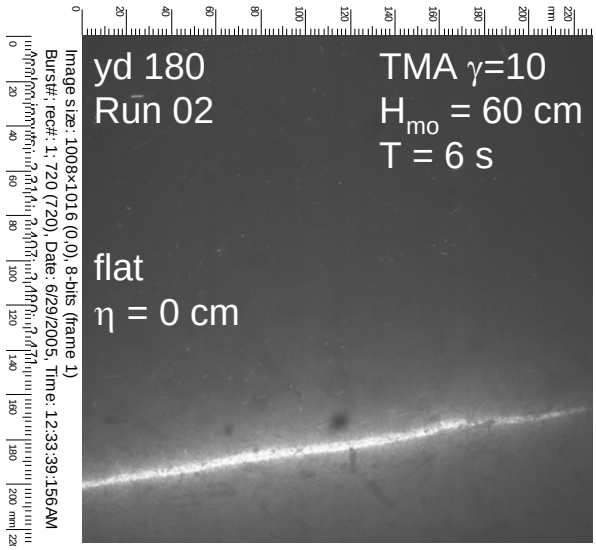

Figure A.11. PIV observations for H_{mo} = 60cm, T = 6s

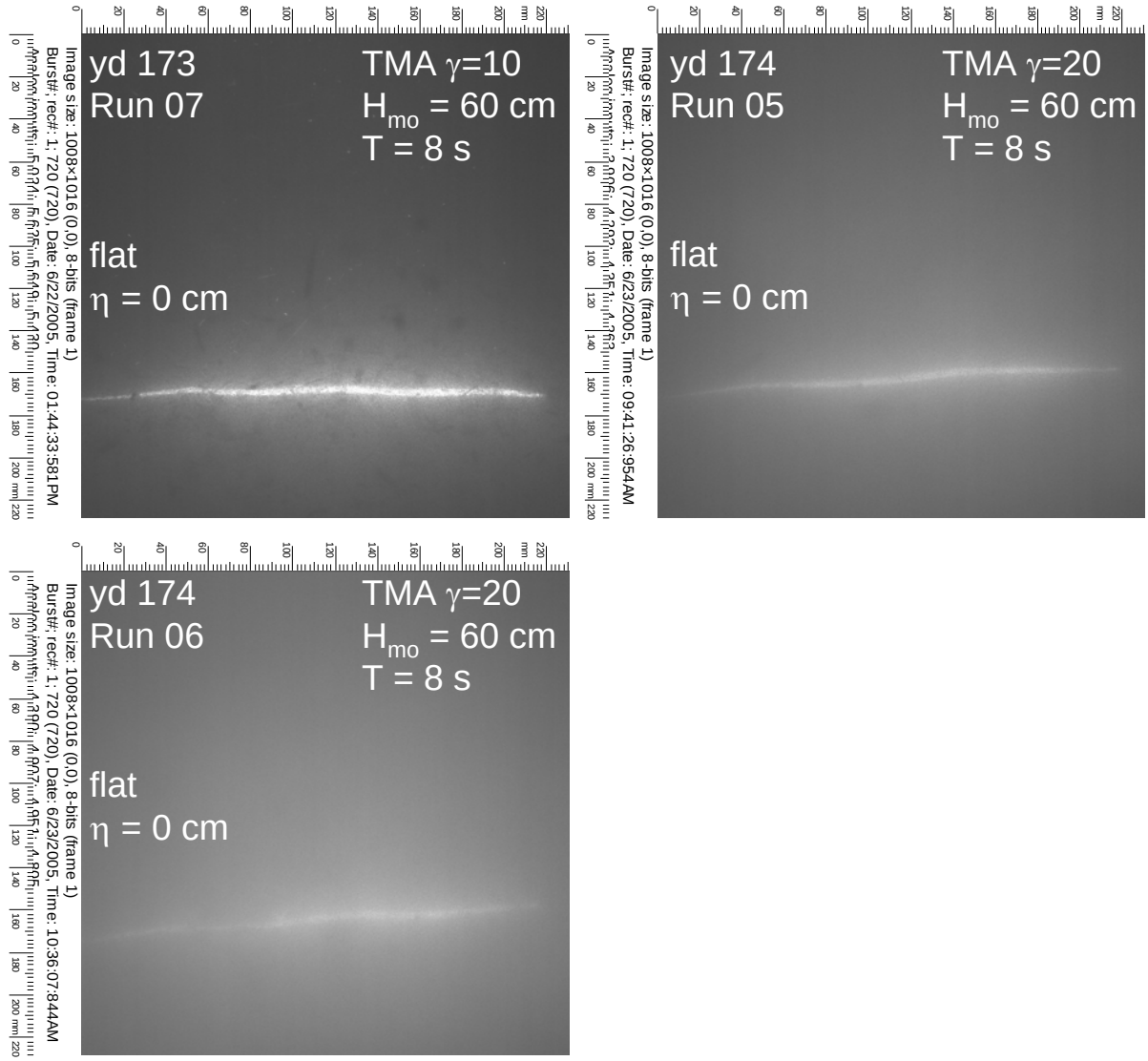

Figure A.12. PIV observations for H_{mo} = 60cm, T = 8s

APPENDIX B

RIPPLE GEOMETRY CALCULATIONS

Run	H_{mo} (cm)	T (s)	u_{rms} (cm/s)	u (cm/s)	Skewness	Asymmetry	lambda (cm)	eta (cm)
173_01_40cm_8s_g10_tma_1a	40	8	23.8	-1.19	0.17	0.396	7.00	0.60
173_02_50cm_4s_g10_tma_1a	50	4	25.2	-3.82	-0.453	-0.192	9.23	0.80
173_03_50cm_6s_g10_tma_1a	50	6	27.5	-2.92	-0.0147	0.107	15.11	0.90
173_04_50cm_8s_g10_tma_1a	50	8	28.6	-2.05	0.034	0.272	10.37	0.20
173_05_60cm_4s_g10_tma_1a	60	4	31.2	-3.99	-0.486	-0.107	23.00	0.00
173_07_60cm_8s_g10_tma_1a	60	8	31.4	-2.27	0.00407	0.444	23.00	0.00
174_01_40cm_4s_g10_tma_1a	40	4	20.5	-3.22	-0.482	-0.174	14.21	1.10
174_02_40cm_6s_g10_tma_1a	40	6	22.6	-2.56	0.0152	0.187	9.01	1.25
174_03_40cm_8s_g10_tma_1a	40	8	24.7	-1.72	0.0811	0.386	8.80	0.55
174_05_60cm_8s_g20_tma_1b	60	8	27.4	-1.15	0.26	0.739	23.00	0.00
174_06_60cm_8s_g20_tma_1c	60	8	27.3	-1.19	0.234	0.741	23.00	0.00
175_02_40cm_8s_g20_tma_hk	40	8	22.5	-1.63	-0.0382	0.219	14.75	2.00
175_03_30cm_8s_g10_tma_1a	30	8	18.5	-1.21	-0.0873	0.159	14.65	1.20
178_03_30cm_8s_g10_tma_1b	30	8	18.8	-1.8	-0.174	0.162	8.60	0.85
178_04_40cm_8s_g10_tma_1a	40	8	22	-1.29	0.0767	0.357	10.15	1.00
178_05_30cm_4s_g10_tma_1a	30	4	15.3	-1.2	-0.299	-0.0685	10.83	1.40
178_06_30cm_6s_g10_tma_1a	30	6	17.1	-2.17	-0.304	0.0386	8.44	1.07
178_07_30cm_8s_g10_tma_1a	30	8	18.6	-1.56	-0.0538	0.257	11.03	0.40
179_04_50cm_4s_g10_tma_1a	50	4	25.7	-3.68	-0.376	-0.22	9.50	0.90
179_05_50cm_6s_g10_tma_1a	50	6	28.2	-3.51	-0.0998	0.0798	10.02	0.90
179_06_50cm_8s_g10_tma_1a	50	8	29	-2.37	-0.00881	0.261	22.80	0.00
180_01_60cm_4s_g10_tma_1a	60	4	30.8	-4.25	-0.492	-0.143	20.80	0.00
180_02_60cm_6s_g10_tma_1a	60	6	32.6	-3.97	-0.0366	0.0469	22.80	0.00
180_05_40cm_4s_reg_1b	40	4	27.3	-3.79	-0.326	0.0407	11.43	1.45
180_07_40cm_8s_reg_1b	40	8	36.6	-3.04	0.284	0.555	15.19	2.30
181_03_30cm_8s_g10_tma_1b	30	8	19.5	-1.62	-0.0671	0.242	11.22	1.15
181_04_30cm_8s_g10_tma_1d	30	8	19.6	-1.65	-0.0648	0.252	12.30	0.95
182_01_30cm_4s_g10_tma_1a	30	4	16.8	-1.14	-0.196	-0.0622	8.62	0.80

Table B.1. Ripple geometry calculations.

Table B.1 continued

182_02_30cm_6s_g10_tma_1a	30	6	18.6	-1.93	-0.107	0.107	15.43	1.10
182_03_30cm_8s_g10_tma_1a	30	8	19.3	-1.27	0.137	0.303	8.98	1.20
182_04_40cm_4s_g10_tma_1a	40	4	22.6	-3.25	-0.334	-0.194	8.42	1.35
182_05_40cm_6s_g10_tma_1a	40	6	24.3	-2.53	0.0343	0.188	8.70	0.70
182_06_40cm_4s_g10_tma_1a	40	4	22.4	-2.83	-0.308	-0.187	12.90	1.30
182_07_40cm_8s_g10_tma_1a	40	8	26	-1.73	-0.0217	0.438	7.60	0.30
182_08_50cm_4s_g10_tma_1a	50	4	27.3	-4.44	-0.458	-0.0665	22.80	0.00
186_01_40cm_4s_g10_tma_1a	40	4	25	-1.7	-0.0506	-0.28	5.50	0.45
186_02_40cm_4s_g10_tma_1b	40	4	22.6	-3.22	-0.338	-0.148	8.37	0.90
186_03_40cm_6s_g10_tma_1a	40	6	24.2	-2.35	0.0278	0.262	7.36	0.73
186_04_40cm_6s_g10_tma_1b	40	6	24.2	-2.56	0.00946	0.248	7.49	0.47
186_05_40cm_8s_g10_tma_1a	40	8	25.7	-2.32	-0.0654	0.493	7.70	0.40
186_06_40cm_8s_g10_tma_1b	40	8	26.3	-2.25	-0.00245	0.45	8.02	0.60
186_07_30cm_4s_g10_tma_1a	30	4	17.7	-1.74	-0.24	-0.0802	7.64	0.68
186_08_30cm_4s_g10_tma_1b	30	4	17.2	-1.67	-0.284	-0.0827	8.07	0.60
186_09_30cm_6s_g10_tma_1a	30	6	18.4	-1.9	-0.141	0.126	8.02	1.30
186_10_30cm_6s_g10_tma_1b	30	6	18.6	-1.92	-0.121	0.142	7.72	0.70
187_01_30cm_8s_g10_tma_1a	30	8	18.6	-1.27	0.0561	0.304	10.41	1.75
187_02_30cm_8s_g10_tma	30	8	19.1	-1.6	0.0538	0.324	11.73	0.40
187_03_50cm_4s_g10_tma_1a	50	4	27.9	-4.37	-0.426	-0.0795	8.21	0.30
187_04_50cm_4s_g10_tma_1b	50	4	28	-4.38	-0.415	-0.0724	6.82	0.95
187_05_50cm_6s_g10_tma_1a	50	6	30.4	-3.86	-0.0156	0.217	22.80	0.00
187_06_50cm_6s_g10_tma_1b	50	6	30.2	-3.83	-0.0392	0.197	22.80	0.00
188_01_30cm_8s_g10_tma_1a	30	8	20.3	-1.64	0.0354	0.25	9.83	1.20
188_02_30cm_8s_g10_tma_1b	30	8	20.3	-1.82	0.0228	0.308	10.70	1.45
188_03_40cm_4s_g10_tma_1a	40	4	22.9	-3.32	-0.35	-0.158	13.41	0.80
188_04_40cm_4s_g10_tma_1b	40	4	22.7	-3.58	-0.416	-0.122	6.43	0.95
189_01_40cm_8s_g10_tma_1a	40	8	25.6	-2.1	-0.0131	0.541	9.62	1.30

Table B.1 continued

189_02_40cm_8s_g10_tma_1b	40	8	26.2	-1.73	0.0508	0.529	10.51	0.65
189_05_60cm_4s_g10_tma_1a	60	4	33.4	-4.74	-0.386	0.0000353	22.80	0.00
189_06_60cm_4s_g10_tma_1b	60	4	33.1	-4.56	-0.38	0.0518	22.80	0.00
192_01_30cm_4s_g10_tma_1a	30	4	17.6	-0.49	-0.0505	-0.00574	11.32	0.80
194_01_30cm_4s_g10_tma_1a	30	4	17.3	-1.55	-0.269	-0.0446	7.34	0.80
194_02_30cm_6s_g10_tma_1a	30	6	18.4	-2.33	-0.272	0.13	9.70	0.80
194_03_30cm_8s_g10_tma_1a	30	8	20	-1.08	0.256	0.369	8.35	1.35
194_04_40cm_4s_g10_tma_1a	40	4	23.2	-3.54	-0.287	-0.0754	9.55	0.42
194_05_40cm_6s_g10_tma_1a	40	6	24	-3.01	-0.0721	0.262	11.46	1.50
194_06_40cm_8s_g10_tma_1a	40	8	25.2	-1.25	0.245	0.625	7.05	0.60
194_07_40cm_4_8s_reg_1a	40	8	31	-3.38	0.064	0.589	11.10	0.35
194_08_40cm_4_8s_reg_1b	40	8	35.2	-3.07	0.192	0.697	22.80	0.00
196_01_30cm_4_8s_reg_1a	30	8	26.5	-1.42	0.176	0.467	8.05	0.55
196_03_50cm_4s_g10_tma_1b	50	4	26.9	-4.18	-0.446	-0.0567	8.84	0.80
196_04_50cm_4s_g10_tma_1c	50	4	27.1	-4.41	-0.43	-0.0765	16.84	1.45
196_05_40cm_4s_g10_tma_1a	40	4	22.4	-3.38	-0.303	-0.0819	9.12	1.05
196_06_50cm_6s_g10_tma_1a	50	6	30	-3.62	-0.0504	0.231	15.80	0.95
197_07_50cm_8s_g10_tma_1a	50	8	31.7	-1.71	0.164	0.484	9.34	0.60
197_08_30cm_6s_g10_tma_1a	30	6	18.2	-2.25	-0.252	0.125	9.90	0.70
197_09_60cm_4s_g10_tma_1a	60	4	32.2	-4.55	-0.423	-0.049	22.80	0.00

APPENDIX C

SEDIMENT ANALYSIS

Sediment analysis data was obtained from Jason Magalen of Oregon State University.

Sieve	d (mm)
40	0.420
50	0.300
60	0.250
65	0.208
100	0.149
140	0.106

Table C.1. Sediment sieve sizes.

Bay	D (mm)
3	0.227
5	0.226
7	0.228
9	0.223
10	0.226
12	0.218

Table C.2. Median sediment grain sizes.

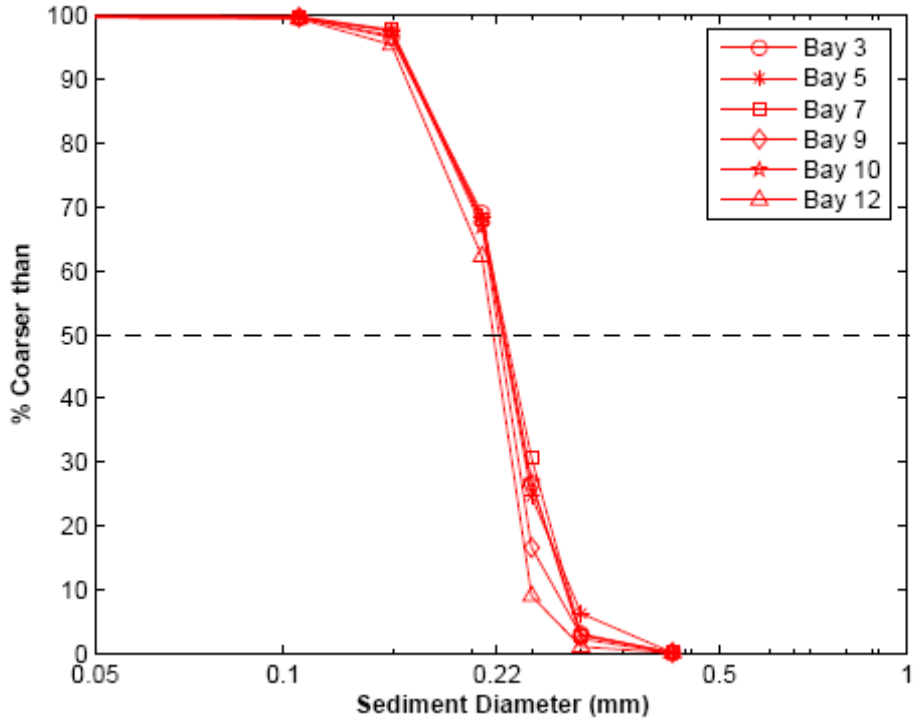

Figure C.1. Median sediment grain size analysis.

BIBLIOGRAPHY

Clifton, H. E., Wave-formed sedimentary structures--A conceptual model, in *Beach and Nearshore Sedimentation*, edited by R. A. Davis Jr. and R. L. Ethington, *Spec. Publ. SEPM Soc. Sediment. Geol., 24*, 126 – 148, 1976.

Clifton, H. E., and J. R. Dingler, Wave-formed structures and paleoenvironmental reconstruction, *Mar. Geol., 60*, 165 – 198, 1984.

Crawford, A. M., and A. E. Hay, Linear transition ripple migration and wave orbital velocity skewness, *J. Geophys. Res., 106(C7)*, 14,113 – 14,128, 2001.

Hay, A. E., and T. Mudge, Principal bed states during SandyDuck97: Occurrence, spectral anisotropy, and the bed state storm cycle, *J. Geophys. Res., 110*, C03013, doi:10.1029/2004JC002451, 2005.

Thornton, E. B., and R. T. Guza, Transformation of wave height distribution, *J. Geophys. Res., 88(C10)*, 5925 – 5938, 1983.

Wiberg, P. L., and C. K. Harris, Ripple geometry in wave-dominated environments, *J. Geophys. Res., 99*, 775 – 789, 1994.